Potential vorticity structure of Titan's polar vortices from Cassini CIRS observations

Jason Sharkey [a],*, Nicholas A. Teanby [a], Melody Sylvestre [a], Dann M. Mitchell [b], William J.M. Seviour [b,e], Conor A. Nixon [c], Patrick G.J. Irwin [d]

[a] School of Earth Sciences, University of Bristol, Wills Memorial Building, Queens Road, Bristol BS8 1RJ, UK
[b] School of Geographical Sciences, University of Bristol, Bristol, BS8 1RL, UK
[c] Planetary Systems Laboratory, NASA Goddard Space Flight Center, Greenbelt, MD 20771, USA
[d] Atmospheric, Oceanic, & Planetary Physics, Department of Physics, University of Oxford, Clarendon Laboratory, Parks Road, Oxford OX1 3PU, UK
[e] Global Systems Institute and Department of Mathematics, University of Exeter, Exeter, EX4 4QF, UK

ARTICLE INFO

ABSTRACT

The Cassini mission has provided the best opportunity to date to extensively study the seasonal variation in Titan's atmosphere, with observations spanning almost half a Titan year ($L_s = 293 - 93°$). An important feature in the Titan middle-atmosphere is the formation of a polar vortex. Observations have shown that an initially well-developed northern vortex enriched with trace gas species gradually breaks down after spring equinox as a new vortex emerges in southern winter. Here we use Cassini CIRS observations to derive the temperature and composition of the middle-atmosphere. We use the gradient wind equation to first estimate the mean zonal winds, and then the Potential Vorticity (PV) throughout Titan's atmosphere over the timespan of the Cassini mission. PV is a useful diagnostic quantity for studying the dynamics of polar vortices because it is materially conserved for adiabatic and frictionless flows, and can be inverted to find all other dynamical fields. Our results show the formation of a strong zonal jet in the winter hemisphere, with wind velocities reaching 220 ms⁻¹, which is consistent with previous studies. An annular PV structure is also observed over the winter poles, whereby a ring of PV encircles a local minima near the pole. Such distributions are often found to be unstable without a restoring force, yet they are seen here in numerous observations in both the northern and southern hemispheres. A comparison with the annular Martian vortices shows that latent heat release from condensation or subsidence-induced adiabatic heating may explain the origin and stability of the annulus. Finally, we investigate the evolution of the size of the vortices and the role of strong PV gradients as a dynamical mixing barrier for trace gas species across the vortex edge. We find that longer lived gases are less confined to the vortex than those with shorter photochemical lifetimes.

1. Introduction

Titan is Saturn's largest moon and shares many similarities with the Earth. The atmospheric composition is approximately 98% nitrogen and 2% methane, with a surface pressure close to 1.5 bar (Fulchignoni et al., 2005). Active photochemistry in Titan's upper atmosphere produces a rich variety of hydrocarbon and nitrile species through the break down of nitrogen and methane into free radicals by ultraviolet light and magnetospheric electrons (Wilson and Atreya, 2004; Lavvas et al., 2008; Krasnopolsky, 2009; Dobrijevic et al., 2014; Loison et al., 2015; Vuitton et al., 2019). The products of these photochemical reactions subside into the cold stratosphere where they may condense, resulting in varying vertical abundance gradients (Teanby et al., 2009). The strength of enrichment in the stratosphere depends on atmospheric

mixing and transport and also the rate of production of the gases and their photochemical lifetimes, which can vary significantly (Wilson and Atreya, 2004; Vuitton et al., 2019).

Titan is tidally locked to Saturn and orbits the planet with a period of around 16 Earth days with one Titan year equivalent to the orbital period of Saturn - approximately 29.5 Earth years. Titan also orbits with Saturn's obliquity of 26.7°, similar to Earth's 23.5°. As with the Earth, this leads to uneven insolation in the atmosphere throughout the year forming seasons. During Titan's winter the stratospheric temperatures at the winter pole have been observed to be up to 50 K colder than at the equator (Teanby et al., 2019). This large temperature gradient is accompanied by the formation of strong zonal winds and a mid-latitude

---

* Corresponding author.
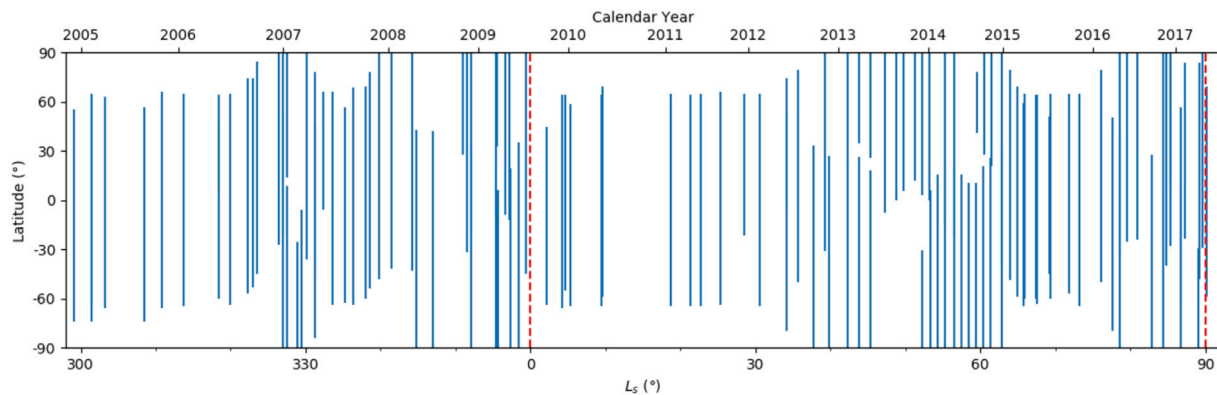 *E-mail address:* js17419@bristol.ac.uk (J. Sharkey).

Fig. 1. Summary of the latitudinal and temporal coverage of the Cassini CIRS 2.5 cm^{-1} MIDIRTMAP observations used in this study. Red dashed lines indicate equinox ($L_s = 0°$) and solstice ($L_s = 90°$). The data initially observes mid northern winter and southern summer, through to summer and winter solstice in the northern and southern hemispheres respectively.

zonal jet in addition to the background superrotation (Achterberg et al., 2008b; Newman et al., 2011), creating the polar vortex. The polar vortex is typically characterised by (i) cold stratospheric temperatures, (ii) a hot stratopause due to subsidence and adiabatic heating and (iii) increased trace gas abundances advected downwards from the photochemically active upper atmosphere. The range of lifetimes of trace gases in the vortex also allows their use as tracers of atmospheric dynamics (Teanby et al., 2008). Atmospheric circulation on Titan is dominated by an upwelling of gas at the summer pole travelling towards the winter pole before subsiding down into the lower atmosphere. This is briefly interrupted around equinox when the circulation is expected to form a two cell system with air upwelling over the equator and travelling towards both poles where subsidence continues to occur. The circulation is then expected to return to a one cell system with upwelling from the summer pole and subsidence over the new winter pole (Hourdin et al., 1995; Lebonnois et al., 2012a; Vinatier et al., 2015).

The Cassini–Huygens mission provides us with the most comprehensive coverage of Titan's atmosphere to date. Orbiting the Saturnian system from 2004 to 2017 ($L_s = 293° − 93°$) and observing Titan on 127 fly-bys, Cassini offers almost half a Titan year of seasonal coverage of both hemispheres (Nixon et al., 2019). On Cassini's arrival Titan was about one third of the way through northern winter, with equinox occurring in August 2009. We therefore have a range of data covering the breakdown of the northern polar vortex in northern summer and the formation of the southern vortex in southern winter (Teanby et al., 2017, 2019; Sharkey et al., 2020). In this study we use infrared data collected by the Composite InfraRed Spectrometer (CIRS) onboard Cassini (Flasar et al., 2004). CIRS is sensitive to many IR-active gases in Titan's atmosphere and so combined with a radiative transfer code offers us the opportunity to investigate the temperature and compositional changes in Titan's atmosphere.

A useful quantity for investigating vortex dynamics is potential vorticity (PV) which can be used as a diagnostic of atmospheric flow. PV is materially conserved under the assumption of adiabatic and frictionless flows, and strong horizontal PV gradients can act as a mixing barrier and are also important for the propagation of Rossby waves (Hoskins et al., 1985; Nash et al., 1996). Previous Titan based studies have also used these assumptions and PV as a means to investigate the polar vortices (Achterberg et al., 2008a; Teanby et al., 2008; Achterberg et al., 2011).

Examining such PV distributions will allow us to examine where the vortex edge is and subsequently the size of the vortex. As the vortex edge is also a mixing barrier to many gases, examining the variation in gas abundance across this region will allow us to better understand how well gases mix across the vortex edge, as a previous study noted a link between gas lifetime and the mixing of the gas outside of the polar

vortex (Teanby et al., 2008). Earlier CIRS studies have investigated the PV distribution in Titan's atmosphere, although they only observed northern winter and did not fully cover polar regions (Achterberg et al., 2008a; Teanby et al., 2008; Achterberg et al., 2011). However, a PV distribution with opposing horizontal gradients was observed, such that a ring of high PV off-pole encircled a local minima near the pole. This 'annulus' structure is not expected to persist as opposing PV gradients should be barotropically unstable (Rayleigh, 1879; Dritschel, 1986). However, Sharkey et al. (2020) found Titan's northern vortex to remain zonally uniform in temperature and composition, suggesting that no large scale barotropic instabilities were observed. With the entire Cassini dataset available, we are able to examine the PV of Titan's vortices with greater spatial and seasonal coverage than any study before. Here we investigate the PV distribution in Titan's atmosphere to determine the origin and stability of Titan's annular vortices as the northern vortex weakens into summer and as the southern vortex grows with the onset of winter. We also investigate the changing size of the vortices and their relative strengths. Finally, by examining the change in gas abundance over the vortex edge we also attempt to describe the polar vortices' abilities to inhibit mixing across their edge.

2. CIRS data

CIRS is a Fourier transform spectrometer capable of recording in the far IR and mid IR (10–1500 cm^{-1}, 1 mm–7 μm). This spectral range includes a large number of IR-active gases in Titan's atmosphere which can be used to derive temperature and composition. CIRS covers this range using three focal planes and a shared telescope and scanning mechanism. The far IR is covered by FP1 (10–600 cm^{-1}), whilst the mid IR is covered by FP3 (600–1100 cm^{-1}) and FP4 (1100–1500 cm^{-1}). CIRS has an apodised spectral resolution which is adjustable between 0.5 and 15.5 cm^{-1}. Here we use the MIDIRTMAP nadir observations which have a spectral resolution of 2.5 cm^{-1} and sufficient spatial coverage and resolution for this study. We use FP3 and FP4 which include both the $\nu_4 CH_4$ band (1240–1360 cm^{-1}) and emissions from a variety of trace gas species. These observations typically probe pressure levels between 10 mbar and 0.001 mbar, although the extent of their reach depends on the latitude and season of each observation, which can shift the location of the contribution functions.

In this study we use MIDIRTMAP observations from all 127 fly-bys to interpret the seasonal evolution of the polar vortices over the entire Cassini mission timespan. Although the number of fly-bys extending coverage all the way to the northern and southern poles is limited to 39 and 32 respectively, inclusion of lower latitude coverage is useful for the deduction of overall seasonal hemispheric trends. Coverage of the CIRS instrument over the Cassini mission is summarised in Nixon et al. (2019). The coverage of the data used in this study is shown in Fig. 1.
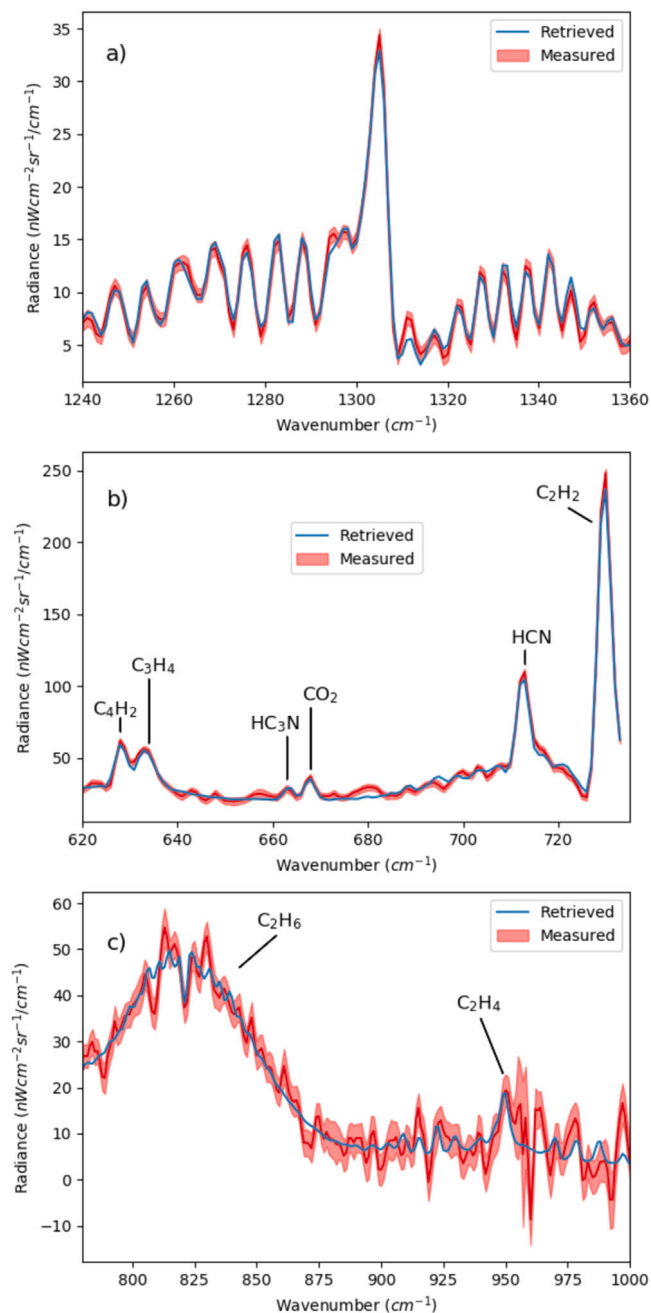
Fig. 2. Example MIDIRTMAP with 2.5 cm^{-1} resolution spectra measured by CIRS at 60°N during northern winter and the fitted spectra retrieved by NEMESIS. (a) ν_4CH$_4$ Methane band in FP4 used for temperature retrievals. (b, c) Multiple IR active gases observed in FP3.

With this data, both poles are generally well covered in time from 2007 ($L_s = 320°$) onwards, with the exception of an approximately 4 year gap between 2009 and 2013 ($L_s = 355° - 40°$) where only equatorial latitudes are observed, until summer solstice in mid-2017 ($L_s = 90°$) where the Cassini mission ended.

We use the DS4000 (version 4.2) calibration provided by the CIRS team in order to improve the signal to noise ratio and remove the background and sky contributions (Jennings et al., 2017). To further improve the signal to noise ratio, we use the data binning technique outlined in Teanby et al. (2006) which tessellates Titan's surface into equal area hexagonal bins, with a bin size of approximately 3°, with spectra recorded within each bin averaged.

3. Methods

3.1. Radiative transfer

Inversion of the IR spectra to temperature and composition is carried out using the NEMESIS radiative transfer retrieval code (Irwin et al., 2008). NEMESIS uses a correlated-k approximation (Lacis and Oinas, 1991; Pierrehumbert, 2010) based on the constrained iterative nonlinear retrieval method (Rodgers, 1976). In this method, model parameters are iteratively optimised in an attempt to match the measured data without straying too far from the model a priori input. In our forward model we set the abundance of CH$_4$ to 1.48%, the value measured by the GC–MS on the Cassini–Huygens entry probe (Niemann et al., 2010). The vertical apriori profiles of gas species are set to a uniform value, which will be scaled by a factor during the retrieval process, with values taken from previous CIRS-based studies (Flasar et al., 2005; de Kok et al., 2007; Coustenis et al., 2007, 2016). Furthermore we use apriori temperature profiles constructed from multiple CIRS observations including far-IR, limb and nadir observations as detailed in Teanby et al. (2017, 2019), Sylvestre et al. (2020).

The same two-stage retrieval method as described in Sharkey et al. (2020) is used. The method is briefly outlined here. Fixing the CH$_4$ abundance allows continuous temperature profiles to be derived using the ν_4 CH$_4$ band (1240–1360 cm^{-1}) in FP4. These temperature profiles are then used with trace gas emissions from FP3 (600–1100 cm^{-1}) to derive mean trace gas abundances in the atmosphere by scaling the uniform apriori vertical abundance profiles of each gas. As NEMESIS scales each gas profile to best fit the data, there is no vertical resolution in retrieved abundances. Uncertainties on both temperature and compositions are also derived from a combination of a forward model error and variance of the spectra used in the retrieval. Examples of the 2.5 cm^{-1} resolution spectra recorded in these wavenumber ranges can be seen in Fig. 2 and a typical retrieved temperature profile and corresponding contribution functions showing the sensitivity of the ν_4 CH$_4$ band is shown in Fig. 3. The temperature contribution functions typically peak around 1 mbar, with the tails extending downwards to near 5 mbar and upwards to a few nanobar. The peaks can be shifted up to between 0.1 and 0.01 mbar near the winter poles due to increased temperatures near the stratopause. However, even as the retrieved temperatures relax towards the apriori profile, temperatures should still remain reasonable between around 10 - 0.001 mbar as the apriori profiles are constructed from retrieval results from a variety of CIRS observations (Teanby et al., 2017).

3.2. Wind and potential vorticity determination

Calculation of PV requires zonal wind velocities to be known. Following Flasar et al. (2005) we calculate mean zonal winds in Titan's stratosphere using the gradient wind equation which relates the vertical gradient of the zonal wind velocity to the meridional temperature gradient. The gradient wind equation is written

$$\frac{\partial}{\partial z_\parallel}\left(2\Omega u + \frac{u^2}{r\cos\phi}\right) = -\frac{g}{T}\frac{1}{r}\left(\frac{\partial T}{\partial \phi}\right)_p$$

where $\Omega = 4.56 \times 10^{-6}$ s^{-1} is Titan's rotation rate, ϕ is latitude, and g is the altitude-dependent gravitational acceleration, with a surface value of 1.35 ms^{-2}, T is the temperature, r is the radius to the calculated position, $z_\parallel$ is the direction along cylinders parallel to the rotation axis along which the derivative is calculated and u is the zonal wind velocity. The gradient wind equation allows us to calculate winds which are in cyclostrophic balance, whereby the centrifugal accelerations are balanced by the horizontal pressure gradients, which is the case for superrotating atmospheres such as Titan where the Coriolis accelerations are small by comparison (See supplementary info of Flasar et al., 2005 or Read and Lebonnois, 2018). Titan's northern vortex was previously
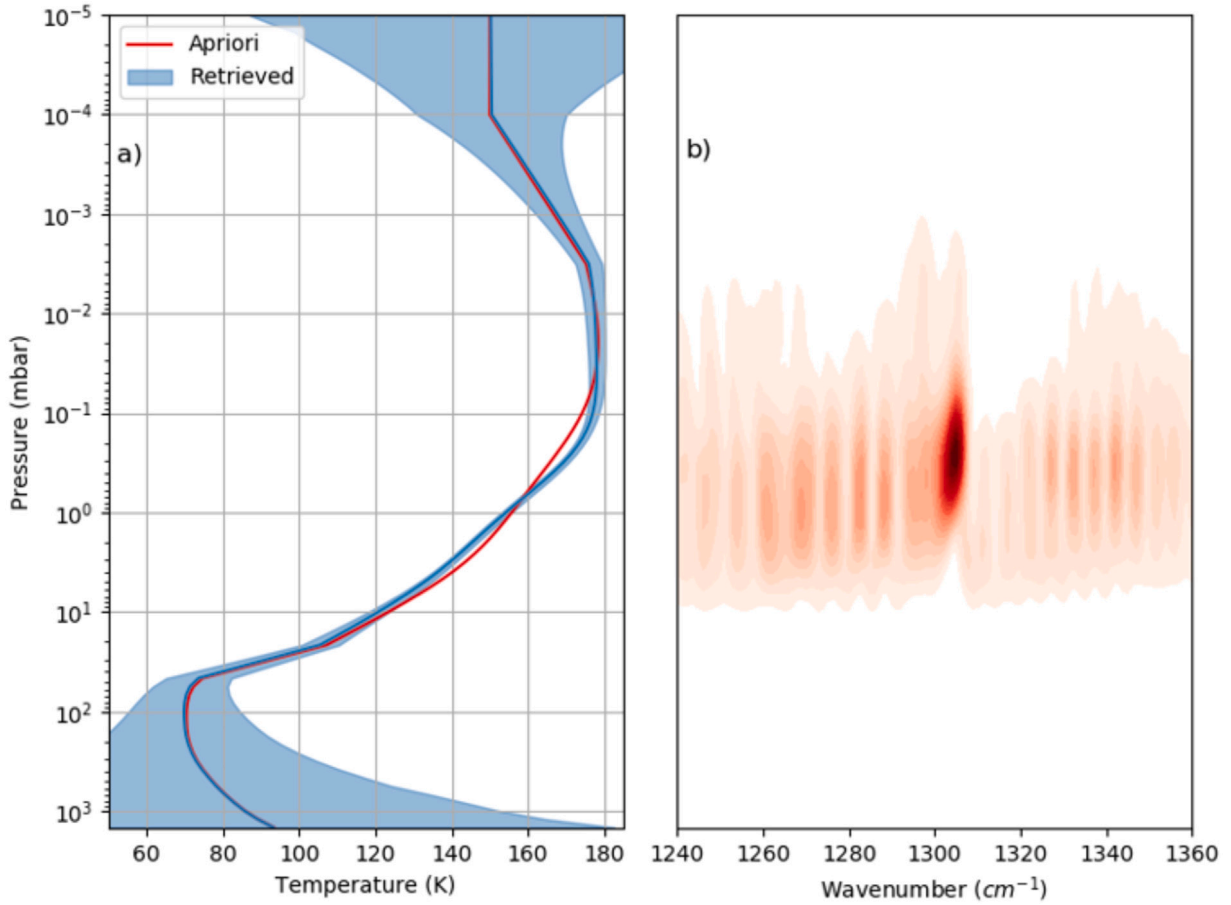
Fig. 3. (a) Continuous temperature profile retrieved from $\nu_4 CH_4$ band at 60°N during northern winter. (b) Contribution functions for the same retrieval. Bright colours indicate regions of sensitivity, which typically provides temperature information between 10 and 0.001 mbar.

shown to exhibit no significant zonal variation (Sharkey et al., 2020) and so we use zonally averaged temperatures to improve the signal to noise. We take the zonal average of temperatures in latitude bins of 1° width. With the binning method outlined in Section 2, this results in around 5 data points per 1° latitude bin on average.

Calculation of the zonal wind from this equation requires a boundary condition to be specified. We choose to use the same condition outlined in Achterberg et al. (2008b), such that the zonal wind speeds at 10 mbar are equal to four times the surface angular velocity, as measured by the Huygens Doppler Wind Experiment (Bird et al., 2005; Folkner et al., 2006). This boundary condition is the addition of a constant value to the calculation, and so variations in this value do not result in changes to the thermal wind structure, and minimal changes to the calculated values. As the derivative is taken parallel to the rotation axis, wind velocities close to the equator are unconstrained by the gradient wind equation, although a new formulation by Marcus et al. (2019) now allows thermal wind calculations over the equator. The gradient wind equation involves temperature gradients, so to avoid the amplification of noise temperatures at each pressure level have been smoothed using a 1 dimensional Gaussian convolution with standard deviation of 3° of latitude.

The potential vorticity (PV) can further be calculated from the retrieved temperatures and derived zonal wind fields. As described in Read et al. (2006) and Teanby et al. (2008) using the hydrostatic approximation, potential vorticity q can be written

$$q = -g\left(f + \xi_\theta\right)\frac{\partial \theta}{\partial p}$$

where $f = 2\Omega \sin\phi$ is the Coriolis parameter, θ is the potential temperature, p is the pressure and ξ_θ is the vertical component of relative vorticity calculated on surface of constant potential temperature,

defined as

$$\xi_\theta = -\frac{1}{r^2 \cos\phi}\frac{\partial}{\partial\phi}\left(ru\cos\phi\right)$$

The potential temperature θ is the temperature a parcel of air would have if it were moved adiabatically to a reference pressure level (Houghton, 2002).

$$\theta = T\left(\frac{p_0}{p}\right)^\kappa$$

where p_0 is the 10 mbar reference pressure, with $\kappa = (c_p - c_v)/c_p = 0.281$ the ratio of heat capacities taken from Teanby et al. (2008). The smoothed temperatures used in the wind calculations, and the resultant winds are both passed onto the PV calculations. As mentioned previously, temperatures are zonally averaged and resampled into 1° latitude bins. Calculated zonal winds (and subsequently PV) resolution is limited by the size of the averaging bins (3°). It should be noted that latitudinal variations in wind or PV on a finer scale than this, if present on Titan, will not be picked up by this method.

4. Results

4.1. Temperature retrievals

The temperature of Titan's middle atmosphere has been studied extensively since the arrival of Cassini. A brief overview of the temperature retrieval results is presented here, but the reader is referred to other studies for greater detail (e.g. Teanby et al., 2019; Sylvestre et al., 2020; Vinatier et al., 2015).

The seasonal variation of temperature in Titan's atmosphere is illustrated in Fig. 4 which shows the zonally averaged temperature
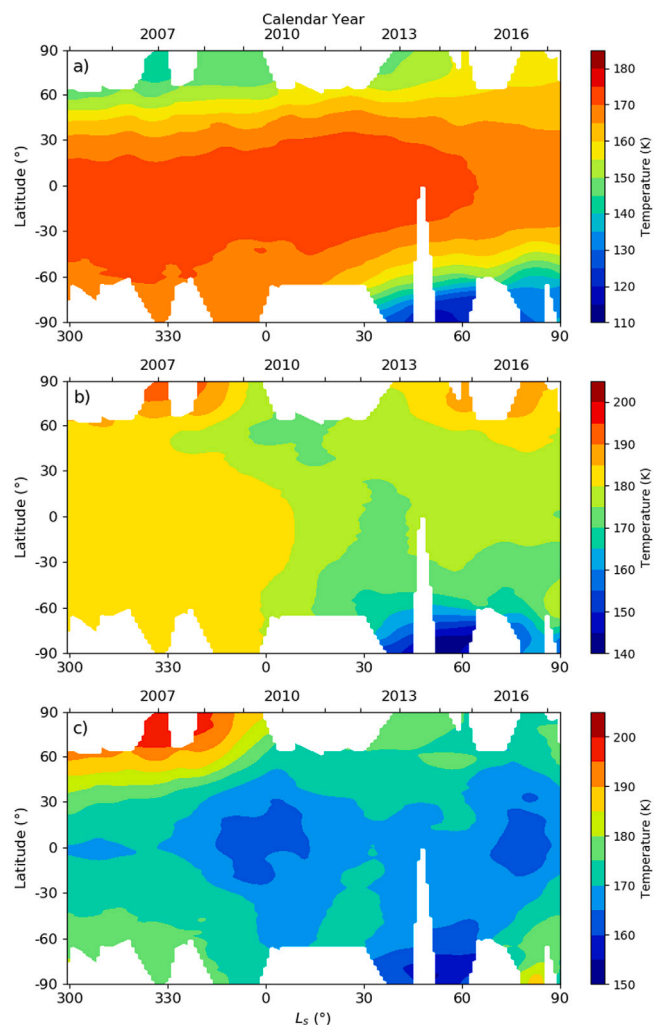
Fig. 4. Seasonal variation of temperature at (a) 1 mbar, (b) 0.1 mbar, (c) 0.01 mbar. The northern pole is initially seen to be cold at 1 mbar, with a hot stratosphere due to adiabatic heating. After equinox, temperatures are seen to drop in the stratosphere, with heating observed at 0.01 mbar near southern winter solstice most likely due to strong adiabatic heating (Teanby et al., 2017).

evolution at the 1, 0.1 and 0.01 mbar level over the Cassini mission. The northern pole is initially seen to be around 30 K colder than the equator at 1 mbar, with a hot stratopause visible at the 0.1 and 0.01 mbar levels due to adiabatic heating. As Titan passes equinox ($L_s = 0°$), the temperatures near the northern pole in the upper stratosphere begin to cool, whilst the southern pole shows a strong temperature decrease from around $L_s = 30°$ onwards. An increase in temperature is observed over the southern winter pole near winter solstice ($L_s = 90°$), most likely due to strong adiabatic heating (Teanby et al., 2017). Cross sections of mean zonal temperature also illustrate these features and are shown in Fig. 5 between 10 and 0.001 mbar across 4 different time periods. Each temperature cross section is the calculated as the average of the temperatures from each observation in the time period. The mean zonal potential temperature for the same time periods is also shown in Fig. 6. As seen in Fig. 3, sensitivity for the ν_4 CH$_4$ band is typically between 10–0.001 mbar depending on the season. In potential temperature coordinates, peak sensitivity (1 mbar) occurs around 350 K, with 0.1 and 0.01 mbar corresponding to approximately 700 K, 1250 K respectively.

4.2. Mean zonal winds

Fig. 7 shows the cross section of mean zonal winds calculated from the average temperatures shown in Fig. 5. In the northern hemisphere, a strong jet is initially inferred at around $L_s = 330°$ and between 0.1 and 0.01 mbar, with peak velocities close to 200 ms^{-1}. As northern winter progresses into summer the winds gradually decrease and the jet vanishes, with maximum wind velocities of around 120 ms^{-1} observed in the northern hemisphere by $L_s = 90°$. After equinox ($L_s = 0°$) the southern mean zonal wind velocities begin to increase rapidly with a strong peak of over 220 ms^{-1} observed at $L_s = 57°$ around 60° south and upwards of 0.1 mbar. By $L_s = 90°$ the maximum winds have decreased slightly moved equatorwards to around 40° south with peak values close to 180 ms^{-1} around 0.1 mbar, forming a strong jet similar to that observed in northern winter.

In Fig. 8 the seasonal change in wind velocities at 1, 0.1 and 0.01 mbar is shown. The largest wind velocities are seen to transition from the northern hemisphere to the southern hemisphere as northern winter passes and southern winter emerges. Solving the gradient wind equation for zonal wind velocity requires the use of the quadratic formula. The discriminant contains the cumulative horizontal temperature gradient along the cylinder for which the calculation is being performed. This value can become negative, turning the discriminant negative, resulting in regions where no wind values can be calculated. This is most likely due to noise in the data combined with taking the derivative of the temperature field. This typically happens high over the winter pole, as seen in the zonal wind cross sections of Fig. 7 and later in the PV distributions in Figs. 9 and 11, although generally winds can be calculated for most fly bys with no issues.

The calculated uncertainty on the mean zonal wind can also be seen in Fig. 8. Uncertainties are obtained by calculating the mean zonal winds N times and taking the standard deviation. In each calculation, the temperatures used include the addition of a random value from a normal distribution with the corresponding temperature error from the retrieval process used as the σ value. Similarly, PV uncertainties are calculated by taking the standard deviation of N PV calculations, with winds and temperatures varied each time with the addition of random noise. In both cases uncertainties were obtained from N = 100 calculations. For the zonal winds, the boundary condition is taken from one measurement in Titan's atmosphere and used across all seasons and latitudes, therefore there is likely to be a significant uncertainty on this value. Whilst it is difficult to quantify the boundary condition uncertainty with no further measurements, its effects on the overall wind uncertainty can readily be calculated for a given value, as the boundary condition is a constant addition to the wind calculation.

4.3. Mean zonal PV

Passing the calculated zonal winds and temperatures into the potential vorticity equation allows inspection of the cross-sectional variation of PV. Fig. 9 shows the PV distributions calculated from the average temperatures and winds shown in Figs. 5 and 7. The seasonal variation of PV can also be seen in both hemispheres in Fig. 10 on 350 K, 700 K and 1250 K isentropic surfaces (approximately 1, 0.1 and 0.01 mbar). PV is plotted on constant potential temperature surfaces as it is conserved on isentropic surfaces for frictionless and adiabatic flows (Waugh, 1997). The dependence of potential temperature on the $(\frac{1}{p})$ factor results in the values of PV increasing rapidly with height. Scaling the PV by a function θ^n, as first suggested by Lait (1994), allows the vertical variation to be significantly reduced, whilst preserving the relative horizontal structure, and conservative properties of PV. They suggest $n = -9/2$ as a suitable value for an isothermal atmosphere, however Teanby et al. (2008) found a value of $-7/2$ to more effectively remove the vertical variation for Titan, and so $n = -7/2$ is used in this study. In all plots, the sign of southern PV values has been flipped to better compare the northern and southern PV distributions.
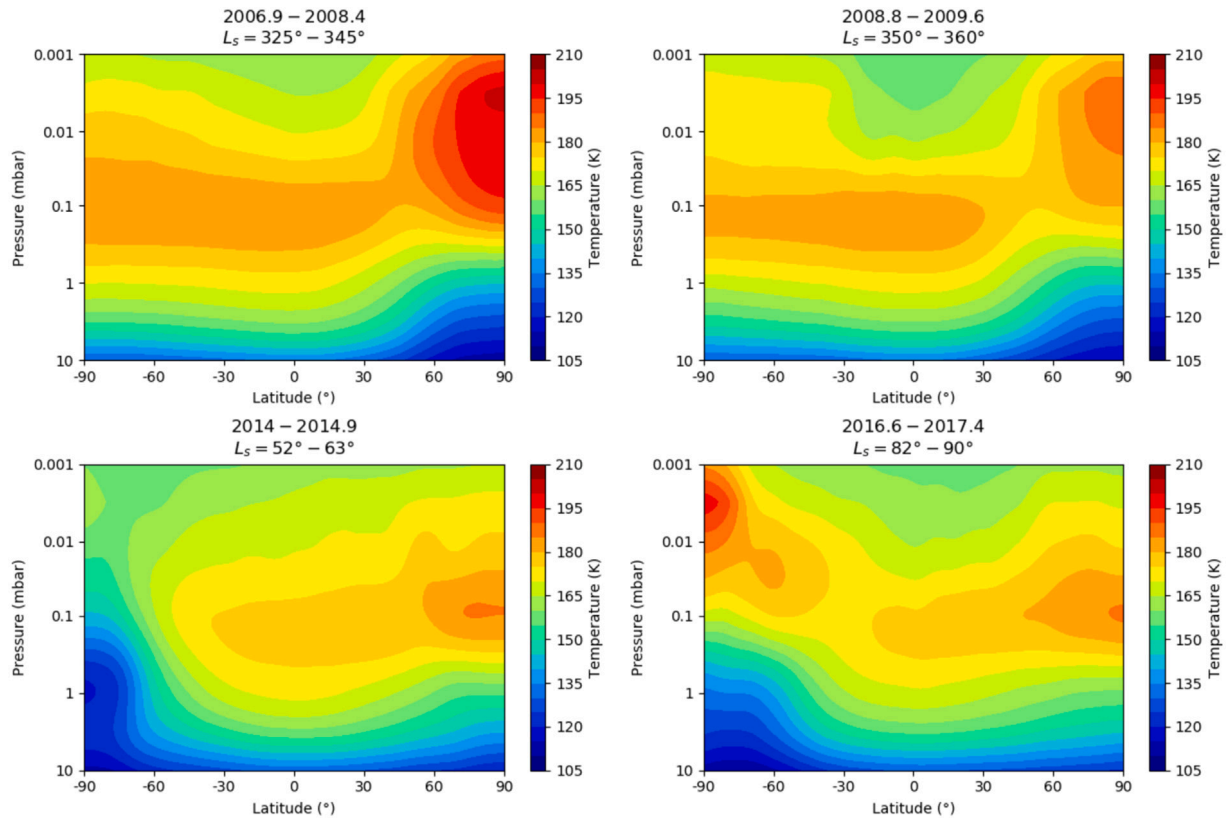
Fig. 5. Cross sections of mean zonal temperatures in Titan's middle atmosphere averaged across different solar longitude time periods. The approximate corresponding calendar year coverage is also shown.
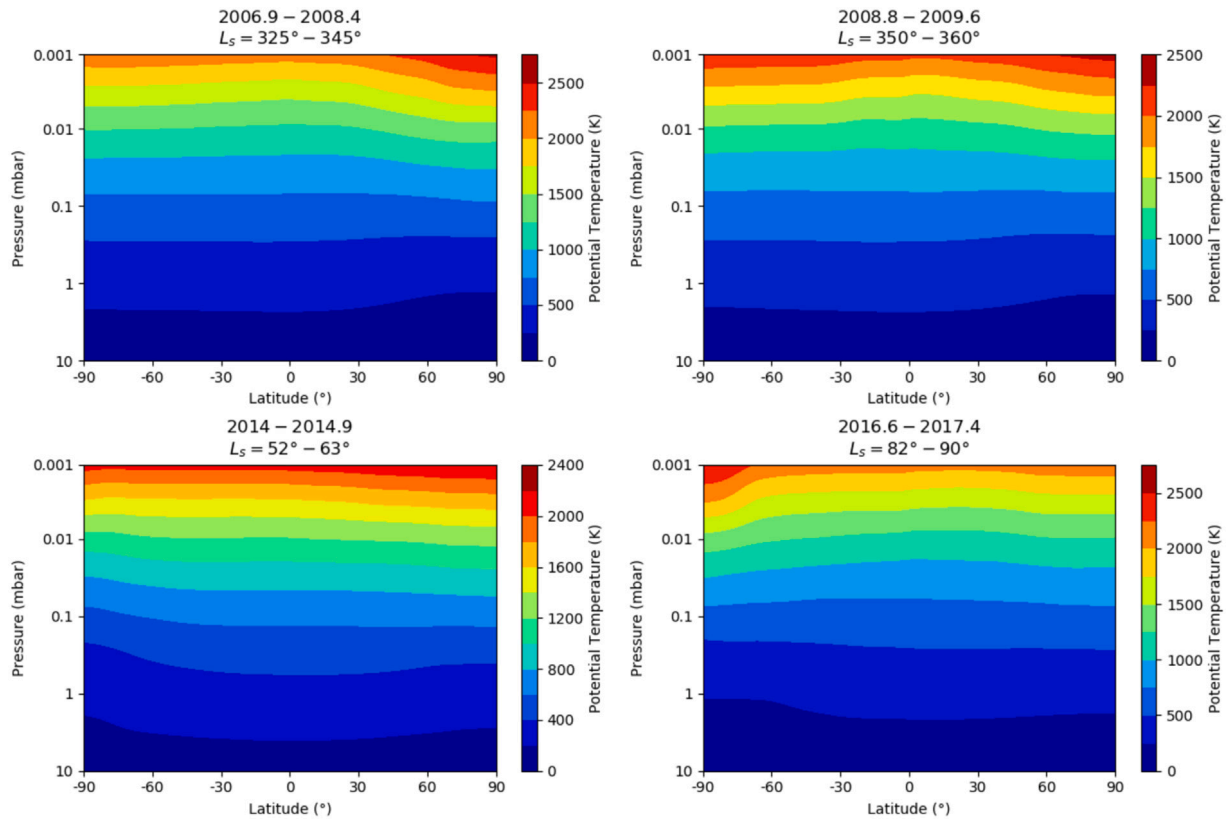

Fig. 6. Mean zonal potential temperature cross sections averaged across the same solar longitudes as Fig. 5 using a reference pressure level of 10 mbar.
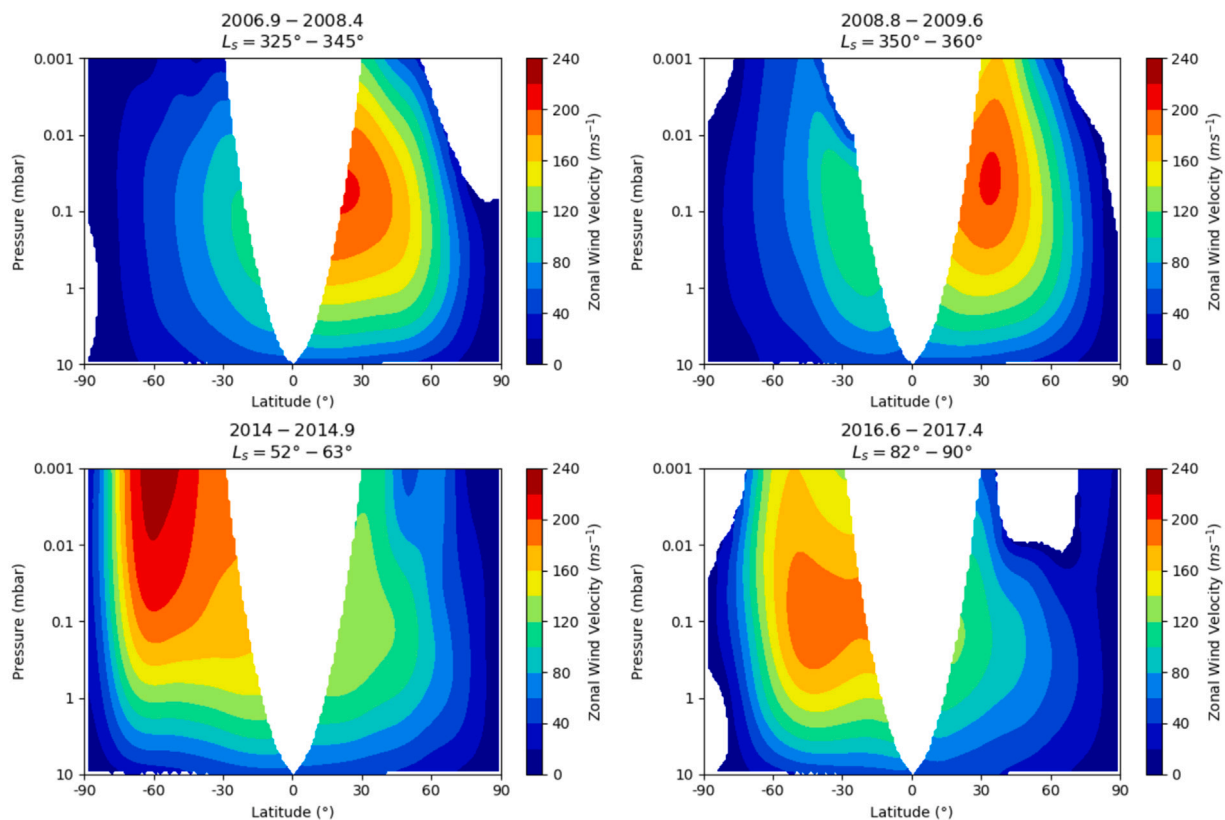
Fig. 7. Mean zonal winds in Titan's stratosphere calculated from the average temperatures shown in Fig. 5. Gradient wind equation is unconstrained over the equator. Other regions are blank where gradient wind equation cannot be calculated, most likely due to noise in data.

During northern winter, maximum PV values are observed in the northern hemisphere with values peaking around 70°. As with the northern winds, the maximum PV values gradually decrease in the north as winter transitions into summer, with PV values close to 0 over the hemisphere by $L_s = 90$. Similarly, in the south after equinox a rapid increase in PV is observed with maximum values found near the pole around $L_s = 57°$ exceeding the maximum values found in the north. By $L_s = 90°$ maximum values have decreased and moved equatorwards, but still exceed those values observed in the north.

Fig. 11 shows the latitudinal PV distributions for both the northern and southern hemispheres over various points in each season using PV units (1 PVU = 10^{-6} $m^2s^{-1}Kkg^{-1}$). In northern winter the PV distribution in the north is seen to exhibit an annulus with a local maximum in PV equatorward of the pole encircling a local minimum over the pole. As the northern hemisphere transitions into summer the maximum PV values steadily decrease and from about $L_s = 40°$ onwards PV monotonically increases towards the pole. By around $L_s = 60°$ the distribution appears to be mostly uniform with no significant increase towards the pole. In the southern hemisphere, before equinox the vortex has not developed and the PV distribution is flat. After equinox, however, there is a sharp increase in PV, with the maximum value observed over the pole. As winter progresses the maximum PV value decreases and the latitude it occurs at shifts equatorwards, becoming annular from around $L_s = 50°$ onwards. Although the PV values calculated in the south are larger than the north, they are not measured at comparable times in the seasonal cycle. As discussed earlier, strong horizontal gradients in PV imply a barrier to mixing processes and maxima in the gradient can be used as an estimator of the vortex edge. Fig. 12 shows the latitudinal variation of PV and the horizontal PV gradient for selected observations in both the northern and southern hemisphere on the 350 K isentropic surface. The latitude of the maximum PV gradient is seen to shift poleward in the north as winter turns to summer, and equatorwards in the south as winter develops.

4.4. Combining northern and southern vortex observations

The lack of year-round coverage of both the northern and southern vortices makes a comparison between the two difficult as we have observations approximately covering winter and spring in the northern hemisphere, and summer and autumn in the southern hemisphere. In order to better visualise how a typical Titan polar vortex may behave over the course of a year, we combine northern and southern hemisphere data into one vortex. To do so we define a new solar longitude frame, Θ, which is equivalent to L_s for southern observations and $L_s - 180°$ for northern observations. In other words, Θ is the solar longitude from autumnal equinox in each hemisphere. The seasonal coverage provided by each hemisphere in this frame is listed in Table 1. However, it is important to note that due to Saturn's elliptical orbit, perihelion occurs at around $L_s = 279°$ and so Titan's northern winter receives less insolation and is shorter than its southern counterpart. The discrepancy in solar heating between the hemispheres could lead to an asymmetry between the strengths of the winters, and subsequently the polar vortices. Figs. 13 and 14 show the replotting of Figs. 8 and 10 in this new frame.

Seasonal variation of the PV in the vortices can be seen in the leftmost column of Fig. 15. The maximum PV value observed on the 350 K isentropic surface shows a rapid increase and then decrease shortly after equinox, with values peaking at around $\Theta = 45°$. From $\Theta = 90°$ onwards the PV values appear to slowly decrease as the vortex enters late winter and early summer. By $\Theta = 240°$ there appears to be no variation in the maximum PV values, with values remaining constant through the remainder of the year, suggesting there is no sign of the vortex in the PV distributions by this point. A similar distribution is seen in the maximum horizontal gradients observed, again with almost no sign of a strong PV gradient by $\Theta = 240°$. The latitudes of the maximum positive PV gradients indicating the vortex edge show a clear growth in the vortex size, with the earliest observations at around
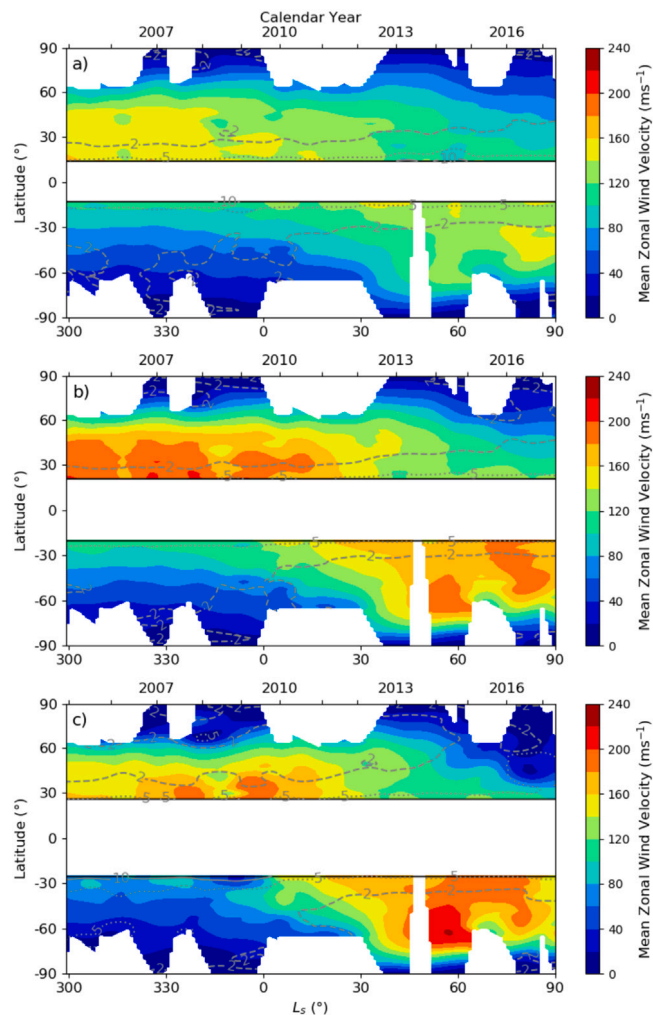
Fig. 8. Mean zonal wind evolution at (a) 1mbar, (b) 0.1 mbar, (c) 0.01 mbar. Uncertainty contour lines shown at 2, 5 and 10 ms^{-1} (dashed, dotted and solid grey lines respectively). Large increase in winds around 60°S due to very cold temperatures in early winter, producing a strong horizontal temperature gradient (Teanby et al., 2017). Gaps in data near the poles are due to lack of coverage, whereas gaps over the equator are due to winds being unconstrained by the gradient wind equation.

Table 1

Solar longitude coverage for northern and southern hemisphere in a new frame combining observations from both hemispheres to represent a single polar vortex. Hemisphere of data and regular solar longitude is shown on the top axis.

Hemisphere	L_s coverage (°)	Θ coverage (°)
Northern	293°–93°	113°–273°
Southern	293°–93°	293°–93°

$\Theta = 45°$ showing the vortex extending to around 15 degrees from the pole, and quickly extending to 40 degrees from the pole by $\Theta = 90°$. The vortex appears to remain fairly uniform in size until around $\Theta = 180°$ where it begins to shrink. By $\Theta = 240°$ the vortex extends to just 20° from the pole, with determination of the vortex edge becoming increasingly difficult due to the mostly flat PV distributions.

4.5. Trace gas abundance variation across the vortex

Investigating the variation in gas composition across the vortex edge will allow us to determine the effectiveness of the vortex as a mixing barrier. We investigate the meridional variation of HCN, C_2H_6, C_2H_2, HC_3N, C_4H_2 and C_3H_4 and the relation between their variation with

Table 2

Photochemical lifetimes of gases used in this study in Titan's atmosphere at 300 km.
Source: Values taken from Vuitton et al. (2019).

Gas	Photochemical lifetime (s)	Titan years
HCN	3.8×10^{11}	408
C_2H_6	4×10^9	4.30
C_2H_2	9.1×10^8	0.98
C_3H_4	1.9×10^8	0.20
HC_3N	8.2×10^7	0.08
C_4H_2	2.6×10^7	0.03

the vortex edge and their photochemical lifetimes, which are listed in Table 2. Fig. 15 illustrates the changing composition of the vortices over the seasons. After equinox we see the vortex becoming enriched in all selected trace gases, with the maximum abundance observed typically peaking sooner for shorter lived gases. For the shorter lived gases (HC_3N, C_4H_2 and C_3H_4) the maximum abundance in the vortex begins to decrease from $\Theta = 90°$ onwards, whereas the longer lived gases either peak at $\Theta = 90°$ and remain constant until $\Theta = 210°$ (C_2H_6) or continuously increase until $\Theta = 210°$ (HCN, C_2H_2). From $\Theta = 210°$ onwards, all trace gases begin to show a sharp decline in maximum abundance in the vortex. As noted in previous studies (Teanby et al., 2009) there is an inverse relationship between trace gas photochemical lifetime and the relative enrichment of the vortex. Examination of the maximum abundance gradients shows a similar trend, with the shortest lived gases exhibiting the largest abundance gradients. All gas abundance gradients are seen to decrease as the vortex becomes depleted in that gas, from $\Theta = 210°$ onwards. Fig. 15 also shows the locations at which the maximum abundance gradients occur, indicating when the gas variation is greatest. All gases shown generally follow the same pattern, with a sharp increase after equinox from between 10–20° from the pole to around 35–50° from the pole by $\Theta = 90°$ in a similar manner to the observed PV distribution. From then on, the peak gas gradients appear to slowly migrate poleward up to $\Theta = 270°$. Beyond this, this abundance distributions have become flat and peak gradient locations do not convey much information.

To better investigate the relationship between peak gas gradient locations and peak PV gradients, we take the average of multiple observations. In Fig. 16 the separation between the vortex edge and the maximum gas variations are shown as a function of photochemical lifetime for various times throughout the year. In early winter as the vortex is forming, the vortex edge lags behind (poleward of) the peak gas variation for all gases. As the vortex begins to grow in size, the edge becomes more in line with the peak gas gradients. Between $\Theta = 50°–90°$ there is equatorward movement of all gas gradients and a more rapid growth of vortex size. By solstice ($L_s = 90°$) the vortex has reached its maximum size and the edge now more closely coincides with most of the gas gradients. The vortex size remains roughly uniform through to $L_s = 180°$, throughout which time we see the shorter lived gases maximum variation drawing back towards the pole, falling in the vicinity of the vortex boundary, indicating that they do not mix greatly across the boundary during this period. However, the two longest lived gases (HCN and C_2H_2) appear to have their peak variation equatorward of the vortex edge. Finally, from $\Theta = 220°$ we see the vortex shrinking in size and weakening (as seen in the maximum PV gradients in Fig. 15). As the vortex weakens, the edge determination becomes more sporadic and the mean edge uncertainty envelopes a larger range of latitudes, during which time all gases show their peak variation creep poleward as the vortex depletes.

5. Discussion

5.1. Mean zonal winds and PV distribution in the middle atmosphere

This study used CIRS nadir data over the entire Cassini mission to estimate zonal winds in both hemispheres. The mean zonal winds calculated here are consistent with values obtained via a variety of methods.
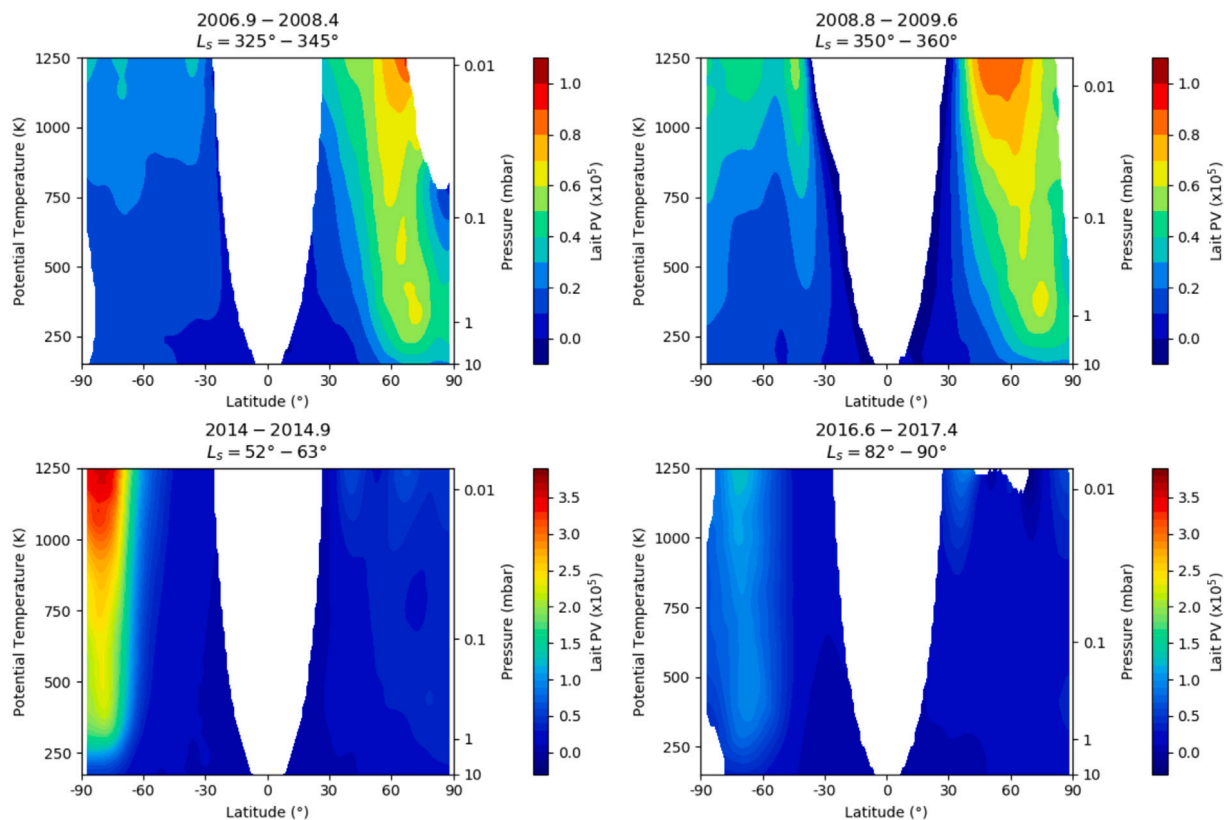
Fig. 9. Mean zonal PV with Lait (1994) rescaling calculated from the average temperatures and winds shown in Figs. 5 and 7. Sign of southern PV has been flipped. The pressure scale is also plotted at the mean potential temperature during each time period. PV is seen to increase towards the winter pole, with a local maxima off-pole and local minima over the pole, forming an annulus.

Previous studies have used earlier CIRS nadir and limb data, and the same gradient wind equation as used in this study, to obtain estimates of zonal wind velocities in the northern winter hemisphere. Achterberg et al. (2008b) found peak wind velocities of around 190 ms^{-1} near 0.1 mbar at 30–50 °N during mid northern winter (L_s = 293–323°). Achterberg et al. (2011) later found similar values for late northern winter (L_s = 347 − 5°). Other methods of measuring wind velocities have also produced similar results. Stellar occultations have provided values of around 180 ms^{-1} at 65°N/S (L_s = 128°) (Hubbard et al., 1993) and 200 ms^{-1} at 55°N (L_s = 290°) (Sicardy et al., 2006). Similarly, Kostiuk et al. (2005) found values of around 190 ms^{-1} at altitudes greater than 200 km (~1–0.1 mbar) near the equator (L_s = 290°) using heterodyne spectroscopy.

Titan General Circulation Models (GCMs) also provide estimates of zonal wind velocities for comparison. Such GCMs have often struggled to accurately reproduce the superrotating winds observed in Titan's middle atmosphere (Lebonnois et al., 2012b; Lora et al., 2019). The Institute Pierre Simon Laplace (IPSL) Titan GCM (Lebonnois et al., 2012a) predicts zonal wind structure and seasonal variation similar to the pattern shown in Figs. 7 and 8 (See Figures 7 and 8 of Lebonnois et al., 2012a). However, the magnitudes of the zonal winds are typically underestimated and peak approximately one order of magnitude in pressure lower (~ 100km lower) compared to previous observations and the values calculated in this study. The Titan Atmospheric Model (TAM) (Lora et al., 2015) more closely matches our observations, with the overall structure of the zonal winds in agreement (See Figure 5 of Lora et al., 2015) although the magnitudes of the peak zonal winds are still underestimated by around 70 ms^{-1} for northern midfall. Similarly, the Titan Weather Research and Forecasting (TitanWRF) model (Newman et al., 2011) reproduces the overall structure of the zonal winds seen in our observations, but slightly underestimates the magnitude and altitude of peak velocities during certain seasons (see

Figures 8 and 9 in Newman et al., 2011). Near L_s = 0°, the peak zonal winds in TitanWRF are around 160 ms^{-1} and occur between 1–0.1 mbar compared to our 200 ms^{-1} between 0.1–0.01 mbar. However, at L_s = 90° our results are in closer agreement with the simulated zonal winds, both of which show peak wind velocities of around 180 ms^{-1}, with the peak GCM winds occurring 1–0.1 mbar and our calculated peak winds around 0.1 mbar.

We also observe for the first time an annulus of maximum PV encircling the poles in both hemispheres in multiple flybys. PV distributions derived from CIRS data have previously suggested an annular PV distribution, as opposing PV gradients in the polar region were observed with a peak in PV occurring around 65°N, but coverage did not extend all the way to the pole and were limited to a few northern winter observations (Achterberg et al., 2008b; Teanby et al., 2008; Achterberg et al., 2011). These results are consistent with the PV distributions calculated in this study, shown in Fig. 11 for the northern vortex in late winter, and the southern vortex approaching winter solstice. These annular PV distributions observed on Titan are not expected to persist, as such distributions have been shown to be barotropically unstable (Dritschel, 1986). However, the annular distribution is consistently seen in the northern hemisphere before equinox, and in the southern hemisphere after around L_s = 50°. There must therefore be a mechanism by which the annular PV distribution is maintained for the vortices. An important factor in discussing the observed PV distributions is the resampled resolution of our data, which is limited to 1° of latitude due to the zonally averaged data used in this study. This resolution is sufficient for analysing the hemispheric behaviour of PV, but will be unable to identify finer scale structure which is often important for barrier mixing processes, as on Earth (Mitchell et al., 2015).

In Figs. 15 and 16 we combine both northern and southern vortex observations to discuss a typical Titan vortex. As mentioned earlier, the eccentricity of Saturn's orbit results in differences in insolation and
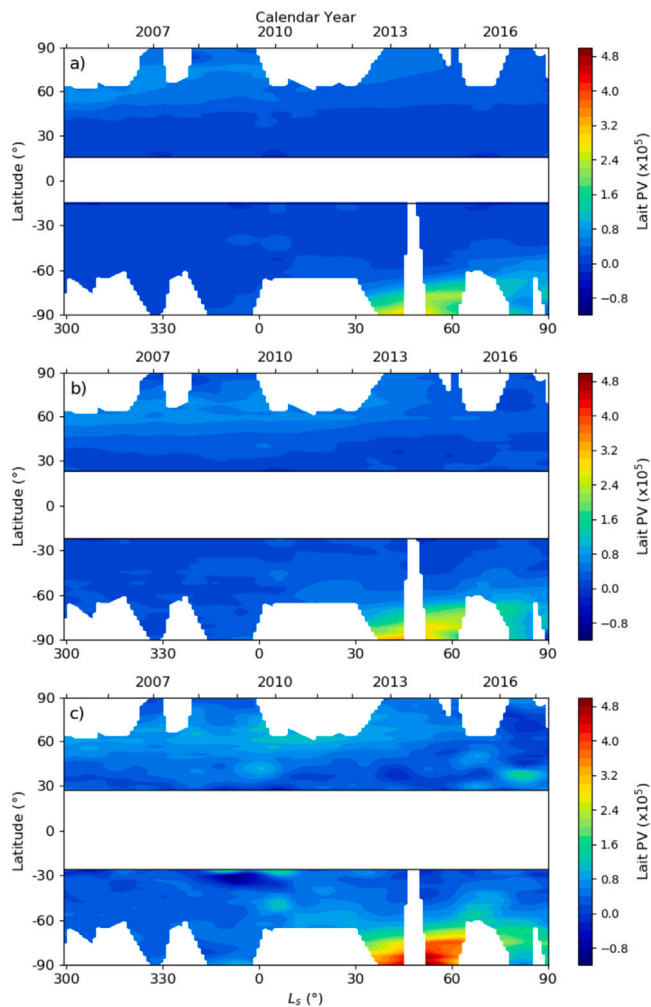
Fig. 10. Mean zonal PV with Lait (1994) rescaling on (a) 350 K, (b) 700 K, (c) 1250 K isentropic surfaces. Sign of southern PV has been flipped. Northern PV is seen to decrease in magnitude as the hemisphere enters summer. Similarly, a strong PV distribution develops in the south shortly after winter begins. In both hemispheres, the PV distribution is seen to exhibit and annular nature.

length of winter between the hemispheres, with the shorter northern winter receiving more insolation than southern winter. Despite this discrepancy, variations in the peak gas abundances and peak PV observed in the vortices appear to show a coherent seasonal trend as seen in Fig. 15, suggesting that the eccentricity of Titan's orbit does not result in significant differences between the polar vortices. Similarly, Jennings et al. (2015) found that the condensate cloud identified by its far-infrared signature at 220 cm^{-1} also shows a coherent seasonal trend between the northern and southern seasons.

5.2. The origin and stability of the annular PV distribution

The polar vortices of Mars have been studied in great depth and also exhibit an annular PV distribution (Banfield et al., 2004; Mitchell et al., 2015; Waugh et al., 2016). Understanding the mechanisms maintaining the annuli in the Martian vortices may help explain the persistence of Titan's annular vortices. Mitchell et al. (2015) suggest that the distribution could possibly be maintained by the circulation, where strong adiabatic heating from the poleward descending air in the global Hadley cell may produce the annular distribution. Titan's winter poles also exhibit strong adiabatic heating from the downward branch of the global circulation, which may help to create the annuli observed.

Toigo et al. (2017) later suggested that the role of CO_2 in the global circulation is responsible. They show, using the MarsWRF GCM, that the annular PV structure can be attributed to the condensation of CO_2 in the Martian atmosphere. The latent heat released during condensation acts to destroy the PV over the winter pole, forming the annular structure (Toigo et al., 2017). Ice clouds of HCN and C_6H_6 have been observed over Titan's southern winter pole (de Kok et al., 2014; Vinatier et al., 2018) and a large condensate cloud was observed by West et al. (2016) over the southern pole using Cassini Imaging Science Subsystem (ISS). It may also be the case that the latent heat released by the condensation of these gases is significant enough to destroy the PV over the pole. However, it remains unclear whether latent heat, adiabatic heating or a combination of the two produce the observed PV annulus on Titan.

More generally, Seviour et al. (2017) went on to investigate the possible factors which determine the stability of the annular Martian vortex. They found that the level of barotropic instability in the Martian vortex is related to the width of the PV annulus, with larger wavenumber components dominating for thinner annuli. Generally, a wider annulus was less likely to produce barotropic instability. Although defining the thickness of the PV profiles observed in this study is not necessarily intuitive, comparing them with the initial profiles used by Seviour et al. (2017) or indeed predicted by Mitchell et al. (2015), they typically show a wider annulus. This may suggest that the PV distributions in Titan's polar vortices are unlikely to produce barotropic instabilities. Recent analysis of zonal variations in the temperature and composition of Titan's northern polar vortex also found no convincing sign of barotropic instability across the vortex (Sharkey et al., 2020). Furthermore, Seviour et al. (2017) showed that sufficiently strong topographical forcing or thermal relaxation timescales longer than the instability timescale could produce a monotonic PV distribution. The former is unlikely to disrupt an annulus on Titan as the topography is relatively flat and not expected to produce waves which can propagate into the stratosphere (Lorenz et al., 2011; Sharkey et al., 2020). Radiative timescales in Titan's atmosphere vary greatly, from longer than 10 Titan years in the troposphere (Strobel et al., 2009) to comparable to a Titan day near 0.1 mbar (Lebonnois et al., 2014; Bézard et al., 2018). The persistence of the annuli suggests that the instability timescales must therefore be longer than these radiative timescales.

A final point on the PV distribution is the variation with altitude. PV in the northern vortex is seen to tilt towards the equator with increasing altitude, whilst the southern vortex shows a less distinct poleward tilt. The PV structure of Earth and Mars's vortices tend to tilt equatorward and poleward respectively, a difference which is attributed to the level of gravity wave activity present, with gravity waves depositing greater energy in Earth's atmosphere than the Martian atmosphere (Mitchell et al., 2015). Gravity waves have previously been identified in Titan's atmosphere (Lorenz et al., 2014), although further investigation into their presence in the polar regions is needed to better understand if and how they alter the vortex.

5.3. The vortex edge as a dynamical mixing barrier

Teanby et al. (2008) first examined the latitudinal variation of trace gas abundance across Titan's northern polar vortex. They found that the longest-lived gases observed in their study (C_2H_2, HCN) showed "tongues" extending equatorward from the vortex. They suggest that gases with such long lifetimes are able to escape the vortex via small scale wave mixing and barotropic instabilities, although trace gases may also escape at lower stratospheric altitudes where the assumption of frictionless flow breaks down and the vortex mixing barrier is less effective, and subsequently be advected equatorward by the descending branch of the mean meridional circulation. These results are consistent with this study, which finds that for the fully developed vortex ($\Theta = 145 - 180$) the longest-lived gases generally exhibit their peak variation outside of the vortex which can be seen in Figs. 15 and 16 showing
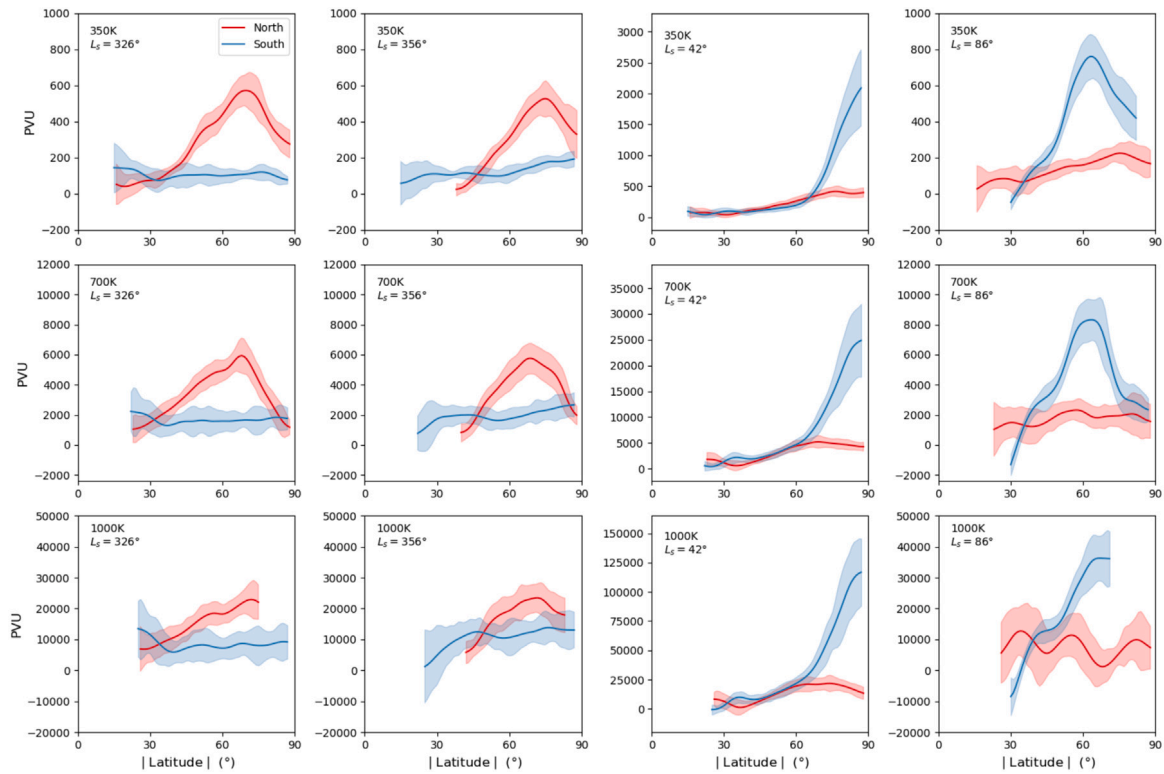
Fig. 11. Latitudinal variation of PV in both hemispheres at different points in the seasonal cycle (columns) and on different isentropic surfaces (rows). Sign of southern PV has been flipped. PV distribution is seen to be flat before the vortex forms in the south and after the vortex breaks up in the north. An annular PV distribution is also seen in both hemispheres.
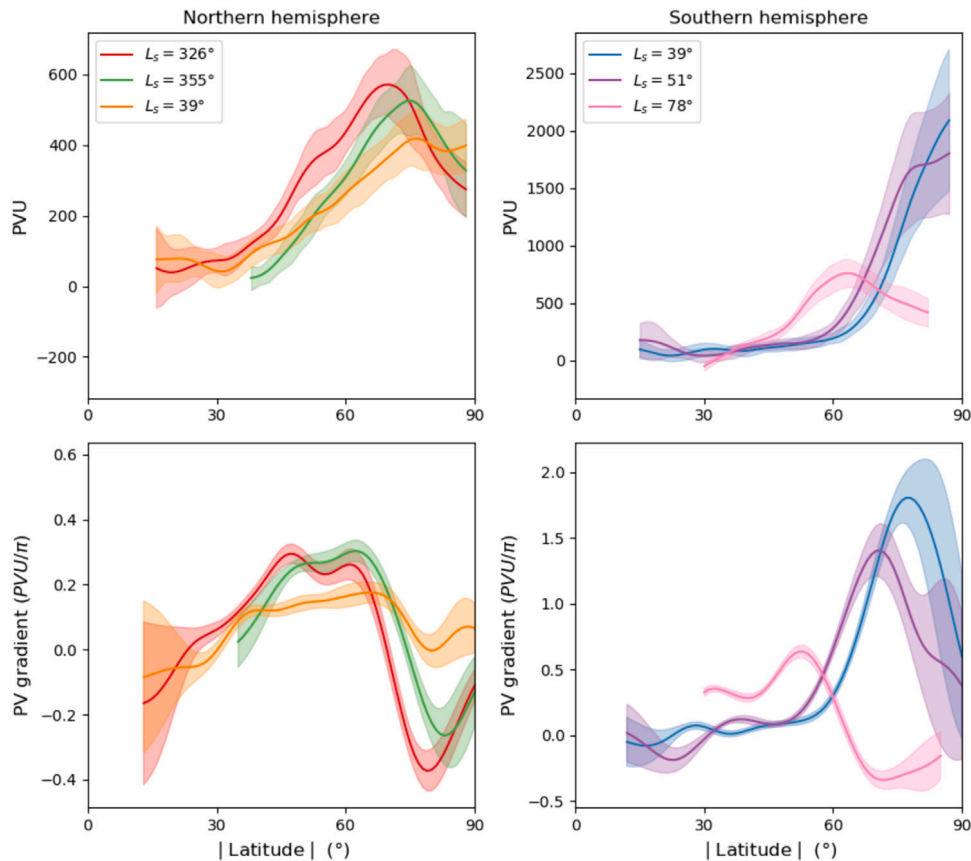

Fig. 12. Seasonal variation of latitudinal PV and PV gradient profiles in both hemispheres on the 350 K isentropic surface. Sign of southern PV has been flipped. Northern PV gradient maxima are seen to move poleward as the summer develops and vortex weakens. Southern PV gradient maxima move equatorward as winter develops and the vortex grows..
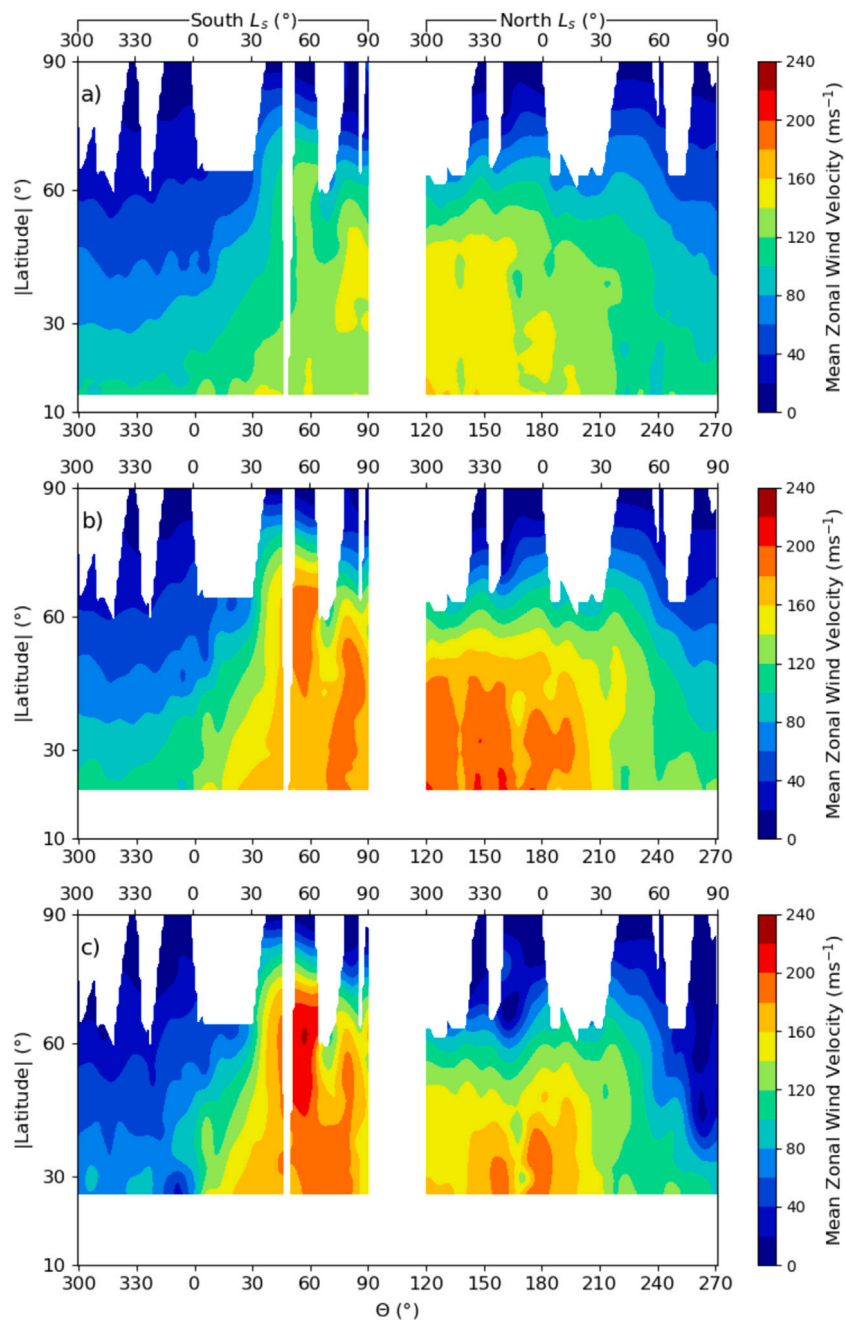
Fig. 13. Mean zonal wind evolution at (a) 1mbar, (b) 0.1 mbar, (c) 0.01 mbar as shown in Fig. 8 in the new reference frame combining both hemispheres.

the latitudinal extent of gas mixing in relation to the vortex edge over different stages in the vortex evolution.

Our results show that there is a close relationship between the seasonal evolution of the PV gradient and the latitudinal variation of trace gas species. Once the vortex appears to have reached its maximum size ($\Theta = 145 - 180$), the longest lived gases exhibit their maximum variation equatorward of the vortex edge, indicating that their mixing across the vortex edge is not greatly inhibited. However, the shorter lived gases are found to vary most in the region of the vortex edge, indicating that these gases are long lived enough to escape the vortex mixing barrier and interact with the main meridional circulation. However, the shorter lived gases vary most in the region of the vortex edge, indicating photochemical lifetimes less than the meridional transport timescale. We also found that even after the vortex had significantly weakened and no longer appeared to present a mixing barrier, maximum variation of trace gas abundance began to regress

poleward. This result is in agreement with Teanby et al. (2019) who found that after the vortex broke up, trace gases did not spread to lower latitudes. They suggest that the main mechanism for stratospheric trace gas depletion is due to the reversed Hadley cell advecting low-latitude trace gas depleted air into the polar mid stratosphere, and increasing insolation causing photochemical loss of trace gases. As mentioned previously, the process of mixing across the vortex barrier can also be enhanced by PV filamentation. However, such fine scale structures are unlikely to be resolved in this study.

6. Conclusion

Using Cassini CIRS nadir data, we investigate the evolution of Titan's polar vortices, observing both the breakup of northern vortex which was well developed on Cassini's arrival ($L_s = 293°$) and the
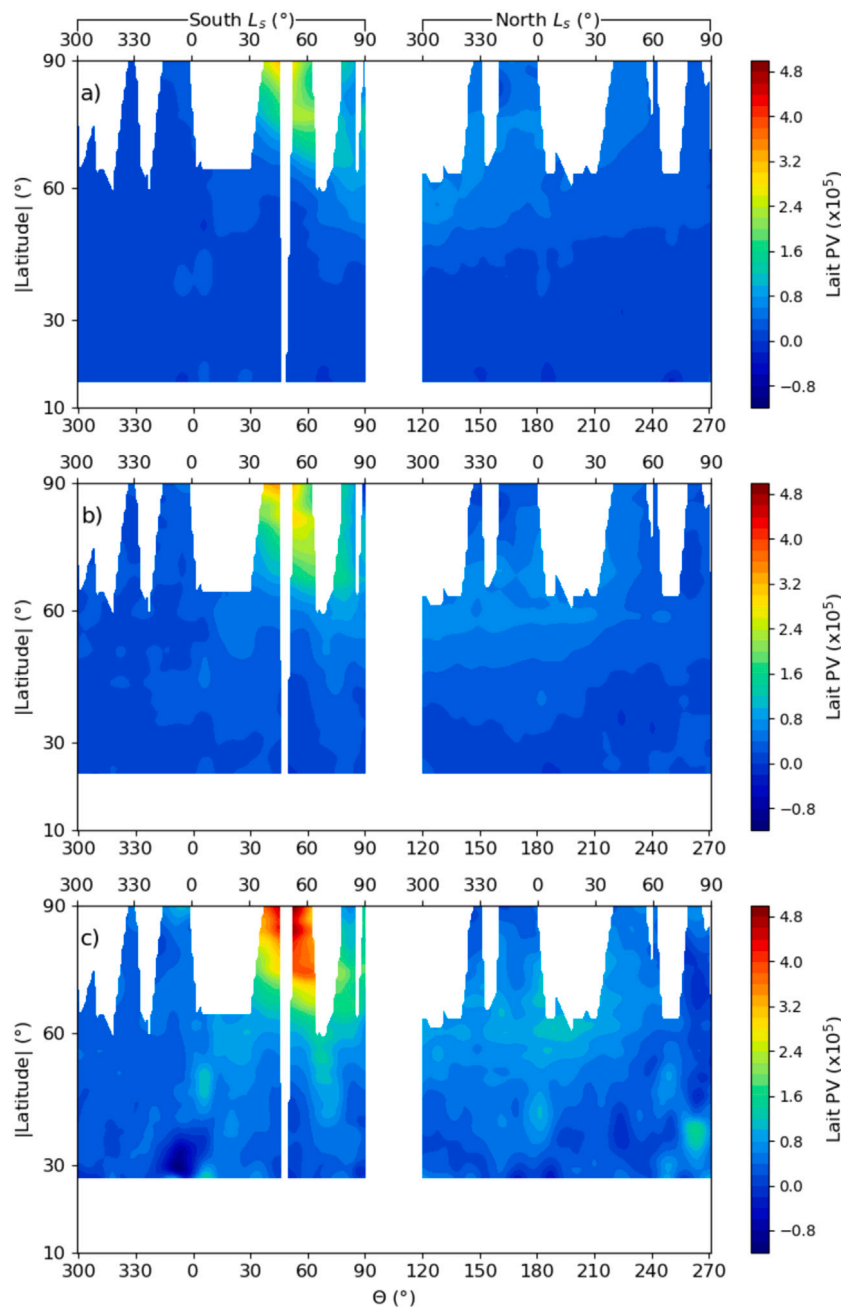
Fig. 14. Mean zonal PV with Lait (1994) rescaling on (a) 350 K, (b) 700 K, (c) 1250 K isentropic surfaces as shown in Fig. 10 in the new reference frame combining both hemispheres. Sign of southern PV has been flipped. Hemisphere of data and regular solar longitude is shown on the top axis.

formation of the southern winter vortex towards the end of the mission ($L_s = 93°$). We use retrieved temperatures to calculate the mean zonal winds in Titan's atmosphere, and subsequently calculate the Potential Vorticity (PV) structure in the polar vortices.

We produce the first mean zonal wind calculations displaying seasonal variations over the entire Cassini mission for Titan's middle atmosphere. Our results initially show the formation of a strong zonal jet in the northern winter hemisphere which gradually migrates to the southern hemisphere as insolation varies, with calculated magnitudes consistent with measurements obtained via a variety of methods. Similarly, we produce seasonal zonal mean PV maps throughout the Cassini mission.

Previous CIRS studies had observed opposing PV gradients near the northern winter pole (Teanby et al., 2008; Achterberg et al., 2008b, 2011). Our results here confirm this distribution, with an annulus

of PV being observed for long periods over both the northern and southern winter poles. Such a PV distribution is not expected to be stable. A comparison with our understanding of the (stable) annular PV distribution on Mars helps us to explain why Titan's also persists for so long. An investigation into the stability of the Martian annulus found that wider annuli tended to show less barotropic instability than thinner annuli, although stability also relied on little topographical forcing and relatively short radiative timescales (Seviour et al., 2017). Titan's topography is relatively flat, and we find Titan has a relatively broad annulus by comparison with Mars. Both of which would help to explain the stability of Titan's annular vortices.

We also discuss the possible causes for the existence and stability of the annular PV structure. Again, studies into the annular nature of the Martian PV aid in understanding Titan's PV. Explanations for Martian annular PV include a forcing mechanism by dynamical heating from the
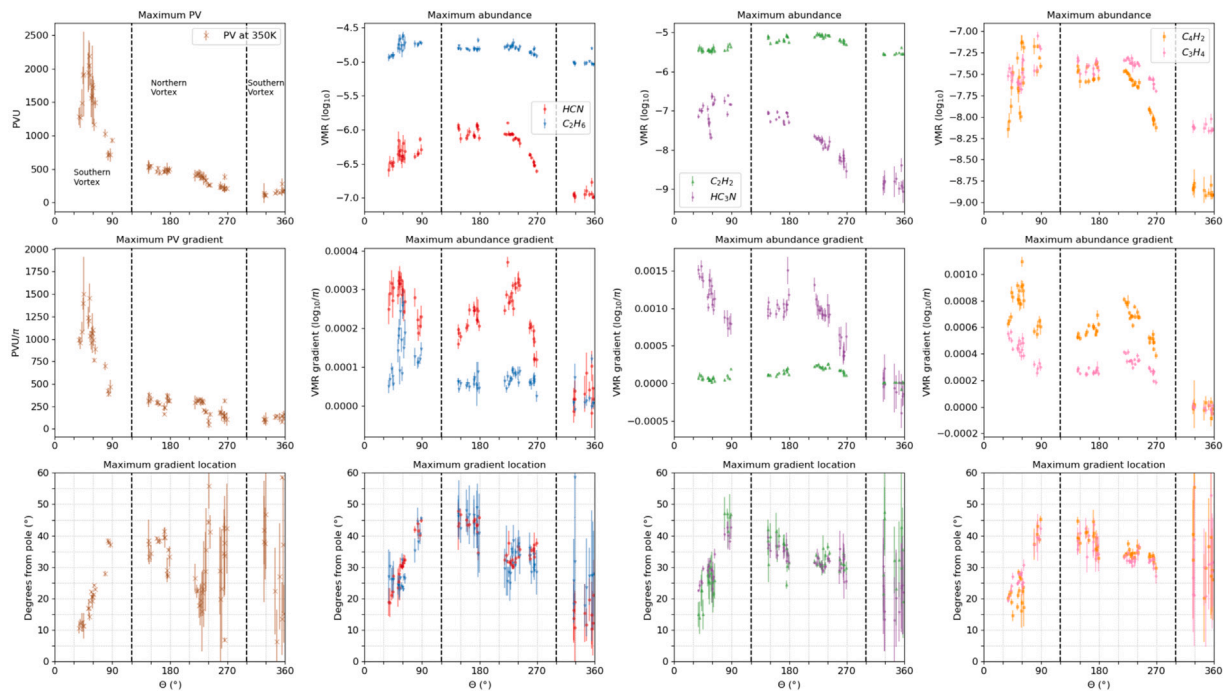
Fig. 15. Seasonal variation of the maximum gas abundance observed in Titan's vortices, the peak meridional gradient of gas abundance and location of peak gradient for HCN, C_2H_6, C_2H_2, HC_3N, C_4H_2 and C_3H_4. Similarly shown is the maximum value of PV observed on the 350 K isentropic surface and the maximum gradient and location (vortex edge). Sign of southern PV has been flipped. Θ is solar longitude relative to autumnal equinox (see text for details). Dashed lines separate data observed in the northern and southern vortices as labelled in the Maximum PV panel (top left).
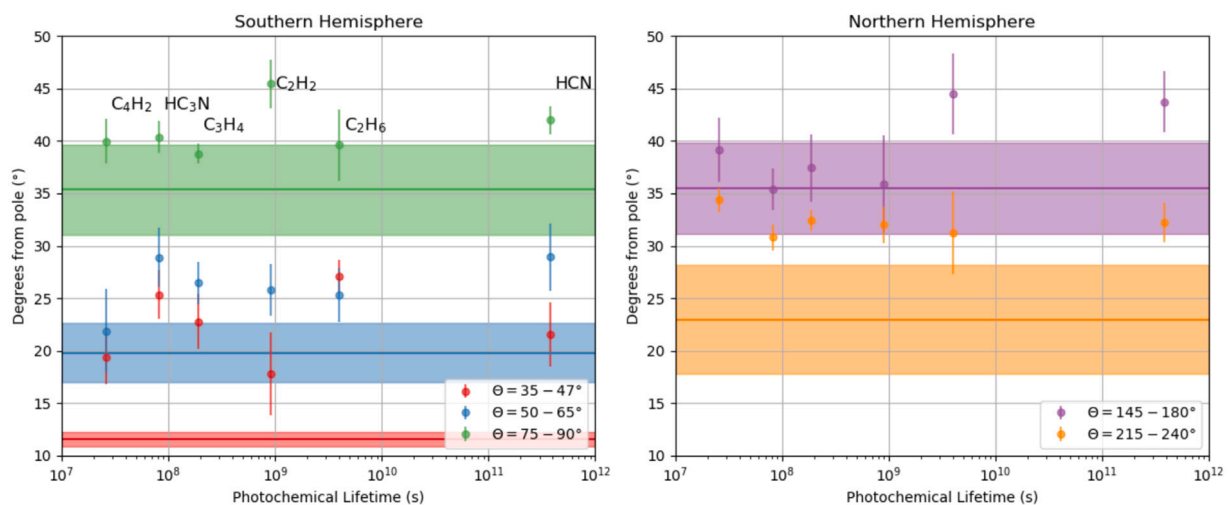

Fig. 16. Mean location of vortex edge (Maximum PV gradient at 350 K) and peak gas abundance variation for selected gases as a function of photochemical lifetime. Transparent envelope represents vortex edge uncertainty, calculated as the deviation of the maximum PV gradient locations.

descending branch of the Hadley cell (Mitchell et al., 2015) and latent heat from condensing CO_2 over the winter pole (Toigo et al., 2017) acting as a PV sink to force the annular structure. Both suggestions may also play a role in producing Titan's annular vortex. Strong adiabatic heating occurs over Titan's winter poles and observed condensation of trace gas species over Titan's southern winter pole may produce latent heat which can play a similar role in destroying PV.

Finally, we investigate the relationship between trace gas abundances and the vortex edge as a dynamical mixing barrier. We find that as winter begins on Titan, the winter pole is rapidly enriched with trace gases, with the formation of the vortex following closely behind. The winter vortex reaches its maximum size by solstice. From here onwards we find evidence that the vortex edge acts as a mixing barrier for trace gas species, inhibiting mixing across between the polar and equatorward air. Longer lived gases are found to extend outside the vortex much more than short lived gases, suggesting that they more readily mix across the barrier. This is likely due to the mixing timescale for the vortex edge, with those gases with photochemical lifetimes greater than the mixing timescale escaping the vortex via small scale mixing across the boundary. As the vortex weakens and dissipates, the now unconstrained gases' gradients do not migrate equatorward, but instead move poleward, most likely due to photochemical loss and the reversed Hadley circulation drawing trace gas depleted air from low latitudes towards the pole.

Acknowledgements

References

Achterberg, R.K., Conrath, B.J., Gierasch, P.J., Flasar, F.M., Nixon, C.A., 2008a. Observation of a tilt of Titan's middle-atmospheric superrotation. Icarus 197, 549–555.

Achterberg, R.K., Conrath, B.J., Gierasch, P.J., Flasar, F.M., Nixon, C.A., 2008b. Titan's middle-atmospheric temperatures and dynamics observed by the Cassini Composite Infrared Spectrometer. Icarus 194 (1), 263–277.

Achterberg, R.K., Gierasch, P.J., Conrath, B.J., Michael Flasar, F., Nixon, C.A., 2011. Temporal variations of Titan's middle-atmospheric temperatures from 2004 to 2009 observed by Cassini/CIRS. Icarus 211, 686–698.

Banfield, D., Conrath, B.J., Gierasch, P.J., Wilson, R.J., Smith, M.D., 2004. Traveling waves in the martian atmosphere from MGS TES Nadir data. Icarus 170 (2), 365–403.

Bézard, B., Vinatier, S., Achterberg, R.K., 2018. Seasonal radiative modeling of Titan's stratospheric temperatures at low latitudes. Icarus 302, 437–450.

Bird, M.K., Allison, M., Asmar, S.W., Atkinson, D.H., Avruch, I.M., Dutta-Roy, R., Dzierma, Y., Edenhofer, P., Folkner, W.M., Gurvits, L.I., Johnston, D.V., Plettemeier, D., Pogrebenko, S.V., Preston, R.A., Tyler, G.L., 2005. The vertical profile of winds on Titan. Nature 438, 800–802.

Coustenis, A., Achterberg, R.K., Conrath, B.J., Jennings, D.E., Marten, A., Gautier, D., Nixon, C.A., Flasar, F.M., Teanby, N.A., Bézard, B., Samuelson, R.E., Carlson, R.C., Lellouch, E., Bjoraker, G.L., Romani, P.N., Taylor, F.W., Irwin, P.G.J., Fouchet, T., Hubert, A., Orton, G.S., Kunde, V.G., Vinatier, S., Mondellini, J., Abbas, M.M., Courtin, R., 2007. The composition of Titan's stratosphere from Cassini/CIRS mid-infrared spectra. Icarus 189, 35–62.

Coustenis, A., Jennings, D.E., Achterberg, R.K., Bampasidis, G., Lavvas, P., Nixon, C.A., Teanby, N.A., Anderson, C.M., Cottini, V., Flasar, F.M., 2016. Titan's temporal evolution in stratospheric trace gases near the poles. Icarus 270, 409–420.

de Kok, R., Irwin, P.G.J., Teanby, N.A., Nixon, C.A., Jennings, D.E., Fletcher, L., Howett, C., Calcutt, S.B., Bowles, N.E., Flasar, F.M., Taylor, F.W., 2007. Characteristics of Titan's stratospheric aerosols and condensate clouds from Cassini CIRS far-infrared spectra. Icarus 191, 223–235.

de Kok, R.J., Teanby, N.A., Maltagliati, L., Irwin, P.G.J., Vinatier, S., 2014. HCN ice in Titan's high-altitude southern polar cloud. Nature 514 (7520), 65–67.

Dobrijevic, M., Hébrard, E., Loison, J.C., Hickson, K.M., 2014. Coupling of oxygen, nitrogen, and hydrocarbon species in the photochemistry of Titan's atmosphere. Icarus 228, 324–346.

Dritschel, D.G., 1986. The nonlinear evolution of rotating configurations of uniform vorticity. J. Fluid Mech. 172, 157–182.

Flasar, F.M., Achterberg, R.K., Conrath, B.J., Gierasch, P.J., Kunde, V.G., Nixon, C.A., Bjoraker, G.L., Jennings, D.E., Romani, P.N., Simon-Miller, A.A., Bézard, B., Coustenis, A., Irwin, P.G.J., Teanby, N.A., Brasunas, J., Pearl, J.C., Segura, M.E., Carlson, R.C., Mamoutkine, A., Schinder, P.J., Barucci, A., Courtin, R., Fouchet, T., Gautier, D., Lellouch, E., Marten, A., Prangé, R., Vinatier, S., Strobel, D.F., Calcutt, S.B., Read, P.L., Taylor, F.W., Bowles, N., Samuelson, R.E., Orton, G.S., Spilker, L.J., Owen, T.C., Spencer, J.R., Showalter, M.R., Ferrari, C., Abbas, M.M., Raulin, F., Edgington, S., Ade, P., Wishnow, E.H., 2005. Titan's atmospheric temperatures, winds, and composition. Science 308, 975–978.

Flasar, F.M., Kunde, V.G., Abbas, M.M., Achterberg, R.K., Ade, P., Barucci, A., Bézard, B., Bjoraker, G.L., Brasunas, J.C., Calcutt, S., Carlson, R., Césarsky, C.J., Conrath, B.J., Coradini, A., Courtin, R., Coustenis, A., Edberg, S., Edgington, S., Ferrari, C., Fouchet, T., Gautier, D., Gierasch, P.J., Grossman, K., Irwin, P., Jennings, D.E., Lellouch, E., Mamoutkine, A.A., Marten, A., Meyer, J.P., Nixon, C.A., Orton, G.S., Owen, T.C., Pearl, J.C., Prangé, R., Raulin, F., Read, P.L., Romani, P.N., Samuelson, R.E., Segura, M.E., Showalter, M.R., Simon-Miller, A.A., Smith, M.D., Spencer, J.R., Spilker, L.J., Taylor, F.W., 2004. Exploring the saturn system in the thermal infrared: The composite infrared spectrometer. Space Sci. Rev. 115, 169–297.

Folkner, W.M., Asmar, S.W., Border, J.S., Franklin, G.W., Finley, S.G., Gorelik, J., Johnston, D.V., Kerzhanovich, V.V., Lowe, S.T., Preston, R.A., Bird, M.K., Dutta-Roy, R., Allison, M., Atkinson, D.H., Edenhofer, P., Plettemeier, D., Tyler, G.L., 2006. Winds on Titan from ground-based tracking of the Huygens probe. J. Geophys. Res. (Planets) 111 (E7), E07S02.

Fulchignoni, M., Ferri, F., Angrilli, F., Ball, A.J., Bar-Nun, A., Barucci, M.A., Bettanini, C., Bianchini, G., Borucki, W., Colombatti, G., Coradini, M., Coustenis, A., Debei, S., Falkner, P., Fanti, G., Flamini, E., Gaborit, V., Grard, R., Hamelin, M., Harri, A.M., Hathi, B., Jernej, I., Leese, M.R., Lehto, A., Lion Stoppato, P.F., López-Moreno, J.J., Mäkinen, T., McDonnell, J.A.M., McKay, C.P., Molina-Cuberos, G., Neubauer, F.M., Pirronello, V., Rodrigo, R., Saggin, B., Schwingenschuh, K., Seiff, A., Simões, F., Svedhem, H., Tokano, T., Towner, M.C., Trautner, R., Withers, P., Zarnecki, J.C., 2005. In situ measurements of the physical characteristics of Titan's environment. Nature 438, 785–791.

Hoskins, B.J., McIntyre, M.E., Robertson, A.W., 1985. On the use and significance of isentropic potential vorticity maps. Q. J. R. Meteorol. Soc. 111 (470), 877–946.

Houghton, J., 2002. The Physics of Atmospheres, third ed. Cambridge Univ. Press.

Hourdin, F., Talagrand, O., Sadourny, R., Courtin, R., Gautier, D., Mckay, C.P., 1995. Numerical simulation of the general circulation of the atmosphere of Titan. Icarus 117, 358–374.

Hubbard, W.B., Sicardy, B., Miles, R., Hollis, A.J., Forrest, R.W., Nicolson, I.K.M., Appleby, G., Beisker, W., Bittner, C., Bode, H.J., Bruns, M., Denzau, H., Nezel, M., Riedel, E., Struckmann, H., Arlot, J.E., Roques, F., Sevre, F., Thuillot, W., Hoffmann, M., Geyer, E.H., Buil, C., Colas, F., Lecacheux, J., Klotz, A., Thouvenot, E., Vidal, J.L., Carreira, E., Rossi, F., Blanco, C., Cristaldi, S., Nevo, Y., Reitsema, H.J., Brosch, N., Cernis, K., Zdanavicius, K., Wasserman, L.H., Hunten, D.M., Gautier, D., Lellouch, E., Yelle, R.V., Rizk, B., Flasar, F.M., Porco, C.C., Toublanc, D., Corugedo, G., 1993. The occultation of 28 SGR by Titan. Astron. Astrophys. 269, 541–563.

Irwin, P.G.J., Teanby, N.A., de Kok, R., Fletcher, L.N., Howett, C.J.A., Tsang, C.C.C., Wilson, C.F., Calcutt, S.B., Nixon, C.A., Parrish, P.D., 2008. The NEMESIS planetary atmosphere radiative transfer and retrieval tool. J. Quant. Spectrosc. Radiat. Transfer 109, 1136–1150.

Jennings, D.E., Achterberg, R.K., Cottini, V., Anderson, C.M., Flasar, F.M., Nixon, C.A., Bjoraker, G.L., Kunde, V.G., Carlson, R.C., Guand ique, E., Kaelberer, M.S., Tingley, J.S., Albright, S.A., Segura, M.E., de Kok, R., Coustenis, A., Vinatier, S., Bampasidis, G., Teanby, N.A., Calcutt, S., 2015. Evolution of the far-infrared cloud at Titan's South Pole. Astrophys. J. 804 (2), L34.

Jennings, D.E., Flasar, F.M., Kunde, V.G., Nixon, C.A., Segura, M.E., Romani, P.N., Gorius, N., Albright, S., Brasunas, J.C., Carlson, R.C., Mamoutkine, A.A., Guandique, E., Kaelberer, M.S., Aslam, S., Achterberg, R.K., Bjoraker, G.L., Anderson, C.M., Cottini, V., Pearl, J.C., Smith, M.D., Hesman, B., Barney, R.D., Calcutt, S., Vellacott, T.J., Spilker, L.J., Edgington, S.G., Brooks, S.M., Ade, P., Schinder, P.J., Coustenis, A., Courtin, R., Michel, G., Fettig, R., Pilorz, S., Ferrari, C., 2017. Composite infrared spectrometer (CIRS) on Cassini. Appl. Opt. 56, 5274–5294.

Kostiuk, T., Livengood, T.A., Hewagama, T., Sonnabend, G., Fast, K.E., Murakawa, K., Tokunaga, A.T., Annen, J., Buhl, D., Schmülling, F., 2005. Titan's stratospheric zonal wind, temperature, and ethane abundance a year prior to huygens insertion. Geophys. Res. Lett. 32 (22).

Krasnopolsky, V.A., 2009. A photochemical model of Titan's atmosphere and ionosphere. Icarus 201, 226–256.

Lacis, A.A., Oinas, V., 1991. A description of the correlated-k distribution method for modelling nongray gaseous absorption, thermal emission, and multiple scattering in vertically inhomogeneous atmospheres. J. Geophys. Res. 96, 9027–9064.

Lait, L.R., 1994. An alternative form for potential vorticity. J. Atmos. Sci. 51 (12), 1754–1759.

Lavvas, P.P., Coustenis, A., Vardavas, I.M., 2008. Coupling photochemistry with haze formation in Titan's atmosphere, Part II: Results and validation with Cassini/Huygens data. Planet. Space Sci. 56, 67–99.

Lebonnois, S., Burgalat, J., Rannou, P., Charnay, B., 2012a. Titan global climate model: A new 3-dimensional version of the IPSL Titan GCM. Icarus 218, 707–722.

Lebonnois, S., Covey, C., Grossman, A., Parish, H., Schubert, G., Walterscheid, R., Lauritzen, P., Jablonowski, C., 2012b. Angular momentum budget in General Circulation Models of superrotating atmospheres: A critical diagnostic. J. Geophys. Res. (Planets) 117 (E12), E12004.

Lebonnois, S., Flasar, F.M., Tokano, T., Newman, C.E., 2014. Titan: Interior, Surface, Atmosphere, and Space Environment. In: Cambridge Planetary Science, Cambridge University Press, pp. 122–157, Ch. The general circulation of Titan's lower and middle atmosphere.

Loison, J.C., Hébrard, E., Dobrijevic, M., Hickson, K.M., Caralp, F., Hue, V., Gronoff, G., Venot, O., Bénilan, Y., 2015. The neutral photochemistry of nitriles, amines and imines in the atmosphere of Titan. Icarus 247, 218–247.

Lora, J.M., Lunine, J.I., Russell, J.L., 2015. GCM simulations of Titan's middle and lower atmosphere and comparison to observations. Icarus 250, 516–528.

Lora, J.M., Tokano, T., Vatant d'Ollone, J., Lebonnois, S., Lorenz, R.D., 2019. A model intercomparison of Titan's climate and low-latitude environment. Icarus 333, 113–126.

Lorenz, R.D., Turtle, E.P., Stiles, B., Le Gall, A., Hayes, A., Aharonson, O., Wood, C.A., Stofan, E., Kirk, R., 2011. Hypsometry of Titan. Icarus 211, 699–706.

Lorenz, R.D., Young, L.A., Ferri, F., 2014. Gravity waves in Titan's lower stratosphere from Huygens probe in situ temperature measurements. Icarus 227, 49–55.

Marcus, P.S., Tollefson, J., Wong, M.H., Pater, Id., 2019. An equatorial thermal wind equation: Applications to Jupiter. Icarus 324, 198–223.

Mitchell, D., Montabone, L., Thomson, S., Read, P., 2015. Polar vortices on Earth and Mars: A comparative study of the climatology and variability from reanalyses. Q. J. R. Meteorol. Soc. 141, 550–562.

Nash, E.R., Newman, P.A., Rosenfield, J.E., Schoeberl, M.R., 1996. An objective determination of the polar vortex using Ertel's potential vorticity. J. Geophys. Res. 101 (D5), 9471–9478.

Newman, C.E., Lee, C., Lian, Y., Richardson, M.I., Toigo, A.D., 2011. Stratospheric superrotation in the TitanWRF model. Icarus 213, 636–654.

Niemann, H.B., Atreya, S.K., Demick, J.E., Gautier, D., Haberman, J.A., Harpold, D.N., Kasprzak, W.T., Lunine, J.I., Owen, T.C., Raulin, F., 2010. Composition of Titan's lower atmosphere and simple surface volatiles as measured by the Cassini-Huygens probe gas chromatograph mass spectrometer experiment. J. Geophys. Res. (Planets) 115, E12006.

Nixon, C.A., Ansty, T.M., Lombardo, N.A., Bjoraker, G.L., Achterberg, R.K., Annex, A.M., Rice, M., Romani, P.N., Jennings, D.E., Samuelson, R.E., Anderson, C.M., Coustenis, A., Bézard, B., Vinatier, S., Lellouch, E., Courtin, R., Teanby, N.A., Cottini, V., Flasar, F.M., 2019. Cassini composite infrared spectrometer (CIRS) observations of Titan 2004–2017. Astrophys. J. Suppl. 244 (1), 14.

Pierrehumbert, R.T., 2010. Principles of Planetary Climate.

Rayleigh, L., 1879. On the stability, or instability, of certain fluid motions. Proc. Lond. Math. Soc. s1-11 (1), 57–72.

Read, P.L., Gierasch, P.J., Conrath, B.J., Simon-Miller, A., Fouchet, T., Yamazaki, Y.H., 2006. Mapping potential-vorticity dynamics on Jupiter. I: Zonal-mean circulation from Cassini and Voyager 1 data. Q. J. R. Meteorol. Soc. 132, 1577–1603.

Read, P.L., Lebonnois, S., 2018. Superrotation on Venus, on Titan, and elsewhere. Ann. Rev. Earth Planet. Sci. 46, 175–202.

Rodgers, C.D., 1976. Retrieval of atmospheric temperature and composition from remote measurements of thermal radiation. Rev. Geophys. Space Phys. 14, 609.

Seviour, W.J.M., Waugh, D.W., Scott, R.K., 2017. The stability of mars's annular polar vortex. J. Atmos. Sci. 74 (5), 1533–1547.

Sharkey, J., Teanby, N.A., Sylvestre, M., Mitchell, D.M., Seviour, W.J.M., Nixon, C.A., Irwin, P.G.J., 2020. Mapping the zonal structure of Titan's northern polar vortex. Icarus 337, 113441.

Sicardy, B., Colas, F., Widemann, T., Bellucci, A., Beisker, W., Kretlow, M., Ferri, F., Lacour, S., Lecacheux, J., Lellouch, E., Pau, S., Renner, S., Roques, F., Fienga, A., Etienne, C., Martinez, C., Glass, I.S., Baba, D., Nagayama, T., Nagata, T., Itting-Enke, S., Bath, K.L., Bode, H.J., Bode, F., Lüdemann, H., Lüdemann, J., Neubauer, D., Tegtmeier, A., Tegtmeier, C., Thomé, B., Hund, F., deWitt, C., Fraser, B., Jansen, A., Jones, T., Schoenau, P., Turk, C., Meintjies, P., Hernandez, M., Fiel, D., Frappa, E., Peyrot, A., Teng, J.P., Vignand, M., Hesler, G., Payet, T., Howell, R.R., Kidger, M., Ortiz, J.L., Naranjo, O., Rosenzweig, P., Rapaport, M., 2006. The two Titan stellar occultations of 14 November 2003. J. Geophys. Res. (Planets) 111 (E11), E11S91.

Strobel, D.F., Atreya, S.K., Bézard, B., Ferri, F., Flasar, F.M., Fulchignoni, M., Lellouch, E., Müller-Wodarg, I., 2009. Titan from Cassini-Huygens. Springer, p. 235, Ch. Atmospheric Structure and Composition.

Sylvestre, M., Teanby, N.A., Vatant d'Ollone, J., Vinatier, S., Bézard, B., Lebonnois, S., Irwin, P.G.J., 2020. Seasonal evolution of temperatures in Titan's lower stratosphere. Icarus 344, arXiv:1902.01841, arXiv e-prints.

Teanby, N.A., Bézard, B., Vinatier, S., Sylvestre, M., Nixon, C.A., Irwin, P.G.J., de Kok, R.J., Calcutt, S.B., Flasar, F.M., 2017. The formation and evolution of Titan's winter polar vortex. Nature Commun. 8, 1586.

Teanby, N.A., de Kok, R., Irwin, P.G.J., Osprey, S., Vinatier, S., Gierasch, P.J., Read, P.L., Flasar, F.M., Conrath, B.J., Achterberg, R.K., Bézard, B., Nixon, C.A., Calcutt, S.B., 2008. Titan's winter polar vortex structure revealed by chemical tracers. J. Geophys. Res. (Planets) 113, E12003.

Teanby, N.A., Irwin, P.G.J., de Kok, R., Nixon, C.A., 2009. Dynamical implications of seasonal and spatial variations in Titan's stratospheric composition. Phil. Trans. R. Soc. A 367 (1889), 697–711.

Teanby, N.A., Irwin, P.G.J., de Kok, R., Nixon, C.A., Coustenis, A., Bézard, B., Calcutt, S.B., Bowles, N.E., Flasar, F.M., Fletcher, L., Howett, C., Taylor, F.W., 2006. Latitudinal variations of HCN, HC_3N, and C_2N_2 in Titan's stratosphere derived from Cassini CIRS data. Icarus 181, 243–255.

Teanby, N.A., Sylvestre, M., Sharkey, J., Nixon, C.A., Vinatier, S., Irwin, P.G.J., 2019. Seasonal evolution of Titan's stratosphere during the Cassini mission. Geophys. Res. Lett. (6), 3079–3089.

Toigo, A.D., Waugh, D.W., Guzewich, S.D., 2017. What causes Mars' annular polar vortices? Geophys. Res. Lett. 44, 71–78.

Vinatier, S., Bézard, B., Lebonnois, S., Teanby, N.A., Achterberg, R.K., Gorius, N., Mamoutkine, A., Guandique, E., Jolly, A., Jennings, D.E., Flasar, F.M., 2015. Seasonal variations in Titan's middle atmosphere during the northern spring derived from Cassini/CIRS observations. Icarus 250, 95–115.

Vinatier, S., Schmitt, B., Bézard, B., Rannou, P., Dauphin, C., de Kok, R., Jennings, D.E., Flasar, F.M., 2018. Study of Titan's fall southern stratospheric polar cloud composition with Cassini/CIRS: Detection of benzene ice. Icarus 310, 89–104.

Vuitton, V., Yelle, R.V., Klippenstein, S.J., Hörst, S.M., Lavvas, P., 2019. Simulating the density of organic species in the atmosphere of Titan with a coupled ion-neutral photochemical model. Icarus 324, 120–197.

Waugh, D.N.W., 1997. Elliptical diagnostics of stratospheric polar vortices. Q. J. R. Meteorol. Soc. 123 (542), 1725–1748.

Waugh, D.W., Toigo, A.D., Guzewich, S.D., Greybush, S.J., Wilson, R.J., Montabone, L., 2016. Martian polar vortices: Comparison of reanalyses. J. Geophys. Res. (Planets) 121, 1770–1785.

West, R.A., Del Genio, A.D., Barbara, J.M., Toledo, D., Lavvas, P., Rannou, P., Turtle, E.P., Perry, J., 2016. Cassini Imaging Science Subsystem observations of Titan's south polar cloud. Icarus 270, 399–408.

Wilson, E.H., Atreya, S.K., 2004. Current state of modeling the photochemistry of Titan's mutually dependent atmosphere and ionosphere. J. Geophys. Res. (Planets) 109, E06002.